International Journal Of
Industrial Electronics Control and Optimization
Print ISSN: 3517-2645
Online ISSN: 3568-2645
Homepage: https://ieco.usb.ac.ir/

Robust Passivity-Based Control with Nonlinear Extended State Observation for Boost DC–DC Converters Feeding Constant Power Loads in DC Microgrids

Mohammad Zabihi Laharami | Hoda Ghoreishy | Seyyed Yousef Mousazadeh Mousavi

1,2 Department of Electrical Engineering, Noshirvani Babol University of Technology, Babol, Iran
3 Department of Electrical Engineering, Faculty of Engineering and Technology, University of Mazandaran, Babolsar, Iran
Corresponding author's email: ghoreishy@nit.ac.ir

Article Info

Article type:
Research Article

Article history:
Received:
Received in revised form:
Accepted:
Published online: ******

Keywords:
Boost DC-DC converter; DC microgrid; Constant power load (CPL); Passivity-based control (PBC); Nonlinear extended state observer (NESO).

ABSTRACT

This paper presents a passivity-based voltage-regulation approach augmented by a nonlinear extended state observer (NESO) for a boost DC-DC converter in a DC microgrid supplying parallel resistive and constant-power loads. The constant-power load exhibits a negative incremental impedance that weakens converter damping and may degrade transient performance or even destabilize the system under load variations, source disturbances, and modeling uncertainties. The boost converter is described by a nonlinear averaged model in which the CPL is represented by its ideal constant-power characteristic within the practical positive-voltage operating region. Building on this model, the controller shapes the closed-loop energy and injects damping for output-voltage regulation, while the NESO estimates lumped disturbances, with the output-voltage-channel disturbance estimate used for compensation through the control law. The main contribution lies in embedding the NESO into a passivity-based control framework to enable online disturbance estimation and active compensation in boost converters feeding parallel resistive and constant-power loads. For the reported gains and tested scenarios, comparative simulations against PI, PBC-only, and ENDO-assisted passivity-based control demonstrate faster voltage recovery, smaller voltage overshoots, and lower tracking-error indices under CPL power variations, resistive-load changes, input-voltage disturbances, and reference-voltage changes.

XVII. Introduction

DC microgrids have attracted considerable attention in recent years because of their high efficiency, modular architecture, and compatibility with renewable energy sources, energy-storage units, and modern electronic loads [1]-[3]. Among the power electronic interfaces commonly used in such systems, the boost DC-DC converter plays an important role in stepping up low source voltages and maintaining the DC-bus voltage under changing operating conditions [4]. This regulation task becomes considerably more difficult when the converter supplies constant-power loads (CPLs). In contrast to conventional resistive loads, CPLs exhibit negative incremental impedance, which reduces the effective damping of the converter and can lead to oscillatory behavior, degraded transient performance, or even instability in the presence of disturbances and parameter variations [5], [6].

The voltage regulation problem is further complicated by the inherent non-minimum-phase characteristic of boost converters. In continuous-conduction mode, the duty-cycle-to-output-voltage dynamics of a boost converter exhibit a right-half-plane zero, which causes an inverse initial response of the output voltage to duty-cycle variations [7], [8]. Consequently, the achievable voltage-loop bandwidth is restricted, and aggressive direct voltage regulation may result in poor transient behavior or even instability [7], [9]. In addition, the negative incremental impedance introduced by CPLs further reduces system damping and may intensify oscillatory behavior and instability [7]. Therefore, robust voltage regulation must simultaneously account for both the bandwidth limitation imposed by the

Copyright © H. Ghoreishy (s).
Publisher: University of Sistan and Baluchestan

intrinsic right-half-plane zero of the boost converter [10] and the destabilizing effect of CPL-induced negative impedance [7].

A topology-based approach to improving step-up converter dynamics was reported in [11], who developed a quadratic CUK-based converter without a right-half-plane zero in the analyzed transfer function. The topology offers high voltage gain and continuous low-ripple input current, with experimental validation using an 80-W prototype. These benefits are obtained with a larger component count than that of a conventional boost converter, including four inductors, six capacitors, and seven diodes. Moreover, the reported load-step experiment concerns resistive loading rather than parallel resistive/CPL operation. Thus, this topology-level approach addresses a different design problem from disturbance-rejection control of a conventional boost converter supplying a CPL.

In practical DC microgrids, the load is often not purely constant power, but instead consists of a parallel combination of resistive and constant-power components [6], [12]. Such a parallel resistive/CPL configuration more faithfully represents applications in which regulated power-electronic devices operate together with conventional passive loads. However, the nonlinear and destabilizing behavior of the CPL component makes voltage regulation more challenging, particularly under load variations, source disturbances, and parameter uncertainties [6], [12], [13].

Various advanced control methods have been investigated for DC converters supplying CPLs, including sliding-mode control (SMC) [14], model predictive control (MPC) [15], adaptive control [16], disturbance observer based approaches [17], and passivity-based control (PBC) [18], [19]. Although these methods have demonstrated promising performance, each approach has certain limitations in practical implementation. SMC is recognized for its robustness against uncertainties, but it may suffer from chattering and switching-induced stress [14]. MPC can explicitly handle system constraints and optimize control objectives, yet it generally requires an accurate prediction model and may impose a considerable computational burden in fast power-electronic systems [15]. Adaptive control can improve robustness against parameter variations, but its transient performance may deteriorate under rapid load changes, external disturbances, or unmodeled dynamics [16]. Similarly, disturbance-observer-based methods can enhance disturbance rejection; however, their effectiveness strongly depends on observer bandwidth selection and estimation accuracy [17]. Against this background, PBC provides an attractive energy-based framework because it exploits the intrinsic energy structure of power converters and enables physically interpretable energy shaping and damping injection. Nevertheless, conventional PBC may still exhibit degraded performance under severe load-side disturbances, input voltage variations, parameter uncertainties, and unmodeled dynamics [18], [19].

In [20] developed a feedback-linearization controller for a grid-connected Siwakoti-H inverter to regulate the flying-capacitor voltage and track the injected-current reference simultaneously. The study includes a PWM implementation and both simulation and experimental validation. However, the authors identify sensitivity to parameter uncertainty: a simulation with 20% errors in the flying-capacitor and inductor values produces small deviations from the references, and additional adaptive or sliding-mode control is suggested to improve robustness. Although the converter and control objectives differ from those considered here, the study highlights the importance of accounting for model uncertainty in nonlinear power-converter control.

To improve robustness, observer-based compensation mechanisms have also been introduced into converter control systems. In several previous studies, nonlinear disturbance observers have been used as auxiliary compensation loops appended to nominal controllers [16], [21]. In [22] combined passivity-based control with nonlinear disturbance observer-based robust control for a boost converter supplying parallel resistive and constant-power loads. Their approach addresses matched and mismatched disturbances and is supported by simulation and experimental results. The disturbance compensation is implemented as an auxiliary correction to the nominal controller. The present study instead investigates a nonlinear extended state observer (NESO) formulation that represents lumped disturbances as additional states and uses the output-voltage-channel disturbance estimate in the implemented passivity-based control law. The distinction therefore concerns the observer formulation and its coupling with the control law, rather than the general combination of PBC and disturbance observation for a boost converter with a parallel resistive/CPL load.

Building on these developments, this paper investigates NESO-assisted passivity-based voltage regulation of a conventional boost converter supplying parallel resistive and constant-power loads. The focus is on the formulation of the extended disturbance states, their coupling with the implemented control law, and the resulting voltage-regulation performance under the tested operating changes. Comparative simulations with PI, PBC-only, and ENDO-assisted PBC controllers assess the proposed implementation under CPL-power variations, resistive-load changes, input-voltage disturbances, and reference-voltage changes. The comparisons are restricted to the reported controller settings and test scenarios.

The main contributions of this paper are summarized as follows:

(i) A NESO-augmented passivity-based control scheme is proposed, in which the nonlinear extended state observer provides online estimates of lumped disturbance

components representing the combined influence of CPL power variations, input-voltage disturbances, parameter uncertainties, and unmodeled dynamics.

(ii) A closed-loop boundedness analysis is provided for the resulting PBC+NESO structure under practical assumptions on the operating region and disturbance behavior.

(iii) Comparative simulation studies demonstrate the effectiveness and robustness of the proposed PBC+NESO method in comparison with PI, PBC-only, and PBC+ENDO controllers.

Section II presents the nonlinear averaged model of the boost converter feeding a parallel resistive-CPL load, characterizes the CPL-induced negative incremental conductance, and derives a nominal-plus-disturbance representation suitable for the subsequent observer-based control design. Section III develops the proposed NESO-based passivity controller and provides the closed-loop uniform ultimate boundedness analysis. Section IV presents the simulation results and performance evaluation. Finally, Section V concludes the paper.

I. System Description and Problem Formulation

This section presents the physical configuration, nonlinear averaged model, and control-oriented formulation of the considered boost-converter subsystem studied as a representative load-side interface stage in a DC microgrid. Fig. 1 shows the system-level architecture of the considered DC microgrid and highlights the studied subsystem connected between the source bus and the load bus. Fig. 2 depicts the detailed electrical schematic of the boost converter and the parallel load structure used for the subsequent derivation of the state-space model.

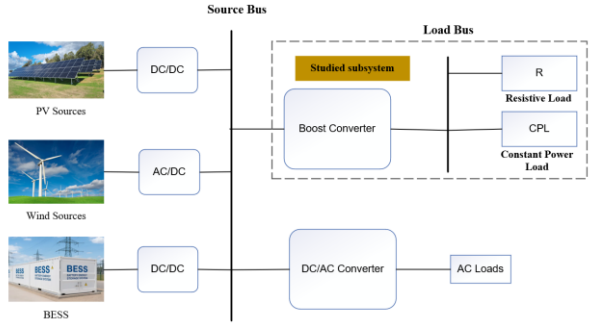


Fig. 1. System-level architecture of the considered DC microgrid.

A. System Description

As shown in Fig. 1, the considered DC microgrid comprises multiple source-side converter-interfaced units connected to a common source bus, while the subsystem studied in this paper is the load-side boost-converter interface supplying a local load bus. The local load bus feeds a parallel combination of a resistive load and an ideal constant power load. The remaining source-side branches are included to clarify the converter's role within the overall microgrid architecture, whereas the modeling and controller design are intentionally focused on the studied converter-level subsystem.

The detailed electrical configuration of the studied subsystem is shown in Fig. 2. It consists of a DC input source V_{in}, a boost converter including the inductor L, diode D, controlled switch with duty ratio u, and output capacitor C, supplying a resistive load R and a constant power load connected in parallel at the load bus. The inductor current and output voltage are selected as the system states, i.e.,

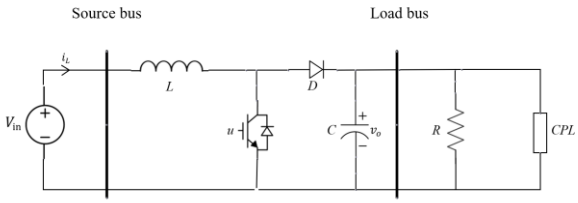


Fig. 2. Electrical schematic of the studied boost DC-DC converter feeding a parallel resistive load and a CPL.

$$x_1 = i_L, x_2 = v_o \tag{1}$$

where i_L denotes the inductor current and v_o represents the output capacitor voltage. The regulated output is $y = x_2$. The control input is the duty ratio of the main switch, defined by $u \in [0,1]$. Accordingly, the factor $1-u$ represents the effective energy transfer interval from the inductor to the output side.

The output load is composed of a resistive part R and a CPL connected in parallel. Hence, the total output current is given by:

$$i_{\text{load}}(x_2, t) = \frac{x_2}{R} + i_{\text{CPL}}(x_2, t) \tag{2}$$

Since the converter is intended to operate in the normal positive-voltage region, the CPL current is modeled by the ideal constant-power relation:

$$i_{\text{CPL}}(x_2, t) = \frac{P_{\text{CPL}}(t)}{x_2}, \qquad x_2 > 0 \tag{3}$$

where $P_{\text{CPL}}(t) > 0$ denotes the instantaneous power demanded by the CPL. Throughout the control-oriented analysis, it is assumed that $x_2 = v_o \geq v > 0$, where v denotes a prescribed positive lower bound on the output voltage. This assumption guarantees that the ideal CPL term remains well defined and avoids the singularity at zero voltage.

B. Nonlinear Averaged Model

Based on the converter circuit shown in Fig. 2, and neglecting the parasitic resistance of the inductor, the nonlinear averaged model of the boost converter is obtained by the standard state-space averaging approach as:

$$\dot{x_1} = \frac{V_{\text{in}}(t)}{L} - \frac{1-u}{L} x_2 \tag{4}$$

$$\dot{x_2} = \frac{1-u}{C}x_1 - \frac{x_2}{RC} - \frac{1}{C}i_{\text{CPL}}(x_2, t) \quad (5)$$

where L and C represent the boost inductor and output capacitor, respectively, and $V_{\text{in}}(t)$ denotes the input voltage.

Substituting the ideal CPL current into the output-voltage dynamics, one obtains:

$$\dot{x_2} = \frac{1-u}{C}x_1 - \frac{x_2}{RC} - \frac{P_{\text{CPL}}(t)}{Cx_2} \quad (6)$$

Therefore, the complete nonlinear averaged model of the boost converter feeding the parallel resistive-CPL load is written as:

$$\begin{cases} \dot{x_1} = \frac{V_{\text{in}}(t)}{L} - \frac{1-u}{L}x_2 \\ \dot{x_2} = \frac{1-u}{C}x_1 - \frac{x_2}{RC} - \frac{P_{\text{CPL}}(t)}{Cx_2} \end{cases} \quad (7)$$

It should be emphasized that the basic averaged model in (7) neglects the inductor parasitic resistance for simplicity. Such effects, together with parameter mismatches and unmodeled dynamics, are incorporated into the control-oriented uncertainty description used in Section III.

C. Incremental Behavior of the Constant Power Load

The CPL exhibits a destabilizing behavior due to its negative incremental conductance, equivalently its negative incremental impedance characteristic. From (3), the incremental conductance of the CPL is obtained as

$$g_{\text{CPL,inc}} = \frac{\partial i_{\text{CPL}}}{\partial x_2} = -\frac{P_{\text{CPL}}(t)}{x_2^2} \quad (8)$$

Since $P_{\text{CPL}}(t) > 0$ and $x_2 > 0$, it directly follows that

$$g_{\text{CPL,inc}} < 0 \quad (9)$$

This means that the CPL behaves as a negative incremental impedance load. For the parallel combination of the resistive load and the CPL, the total incremental load conductance is

$$g_{\text{load,inc}} = \frac{1}{R} + g_{\text{CPL,inc}} \quad (10)$$

Consequently, the total incremental load conductance becomes

$$g_{\text{load,inc}} = \frac{1}{R} - \frac{P_{\text{CPL}}(t)}{x_2^2} \quad (11)$$

Equation (11) shows that an increase in the CPL power demand reduces the effective damping of the output dynamics and may deteriorate the stability margin of the DC microgrid. Hence, in the control-oriented analysis, the same damping-related quantity reappears in Section III through the mean value theorem representation of the ideal CPL term, which yields a state-dependent coefficient admitting a local operating-point interpretation.

D. Control-Oriented Model Representation and Control Objective

For observer and controller design, it is useful to rewrite the nonlinear model in a nominal-plus-disturbance form. Let $V_{\text{in},n}$, R_n, and P_n denote the nominal values of the input voltage, resistive load, and CPL power, respectively. Since the converter operates in the normal voltage region $x_2 \geq \underline{v} > 0$, the ideal CPL term is well-defined over the considered operating domain.

Then, the model can be decomposed as:

$$\dot{x_1} = \frac{V_{\text{in},n}}{L} - \frac{1-u}{L}x_2 + d_1(t) \quad (12)$$

$$\dot{x_2} = \frac{1-u}{C}x_1 - \frac{x_2}{R_nC} - \frac{P_n}{Cx_2} + d_2(x, t) \quad (13)$$

where $d_1(t)$ represents the input-channel disturbance, primarily associated with the deviation of the input voltage from its nominal value and, if desired, any additional current channel modeling mismatch, namely:

$$d_1(t) = \frac{V_{\text{in}}(t) - V_{\text{in},n}}{L} \quad (14)$$

The term $d_2(x, t)$ denotes the lumped output-channel disturbance, including the uncertainty of the resistive load, CPL power variation, unmodeled dynamics, and external disturbances. It can be expressed as:

$$d_2(x, t) = \left[-\frac{x_2}{RC} + \frac{x_2}{R_nC}\right] + \left[-\frac{P_{CPL}(t)}{Cx_2} + \frac{P_n}{Cx_2}\right] + \Delta_{2m}(x, t) \quad (15)$$

where $\Delta_{2m}(x, t)$ represents additional modeling errors and unmodeled dynamics in the output voltage channel.

Therefore, the nominal-plus-disturbance model is compactly given by:

$$\begin{cases} \dot{x_1} = \frac{V_{\text{in},n}}{L} - \frac{1-u}{L}x_2 + d_1(t) \\ \dot{x_2} = \frac{1-u}{C}x_1 - \frac{x_2}{R_nC} - \frac{P_n}{Cx_2} + d_2(x, t) \end{cases} \quad (16)$$

This representation preserves the physical contribution of both the resistive load and the CPL in the nominal dynamics, while collecting parameter mismatches and external perturbations into the disturbance terms $d_1(t)$ and $d_2(x, t)$. However, a more compact formulation is advantageous for the subsequent NESO-based controller synthesis.

Finally, for later use in the observer and controller design, the output voltage dynamics in (13) can be rewritten in the following compact form:

$$\dot{x_2} = \frac{1-u}{C}x_1 + \Phi_v(x, t) \quad (17)$$

where

$$\Phi_v(x, t) = -\frac{x_2}{R_nC} - \frac{P_n}{Cx_2} + d_2(x, t) \quad (18)$$

Similarly, the complete system may be expressed as

$$\begin{cases} \dot{x_1} = \frac{V_{\text{in,n}}}{L} - \frac{1-u}{L}x_2 + d_1(t) \\ \dot{x_2} = \frac{1-u}{C}x_1 + \Phi_v(x, t) \end{cases} \quad (19)$$

In this form, $\Phi_v(x, t)$ contains the nominal load dynamics as well as the lumped output-channel disturbance. Hence, the physical effects of the resistive load and the CPL are not ignored; rather, they are embedded in a compact representation that is suitable for the subsequent nonlinear extended state observer and passivity-based controller design. In the subsequent NESO design, the lumped disturbance terms d_1 and d_2 are treated as extended states to be estimated online, while the nominal resistive-load and CPL dynamics remain explicitly represented in the control-

oriented model. The control objective is to regulate the output voltage to a small neighborhood of a constant reference $V_{ref} > 0$, while maintaining bounded inductor current in the presence of the modeled uncertainties and disturbances.

II. NESO-Assisted Passivity-Based Control Design

This section develops a composite nonlinear controller for the boost converter feeding parallel resistive and constant power loads. The proposed controller combines a passivity-based control law with a nonlinear extended state observer (NESO) to preserve the nominal passive structure, inject additional damping into the voltage channel, and compensate for lumped uncertainties, while counteracting the destabilizing effect associated with the CPL's negative incremental conductance. The controller and observer designs developed below use the nominal-plus-disturbance model in (16), with the disturbance definitions, admissible voltage domain, and control objective given in Section II-D. The incremental-conductance analysis in Section II-C provides the physical interpretation of the CPL-induced damping reduction. The overall control architecture is illustrated in Fig. 3.

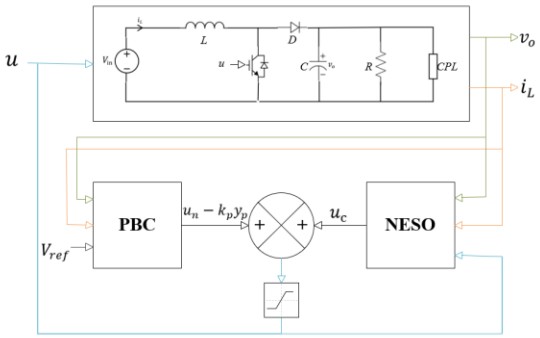


Fig. 3. Composite PBC+NESO control structure for the boost converter feeding parallel resistive and constant power loads.

A. Nominal Passivity-Based Error Dynamics

Define the virtual current tracking error and output-voltage regulation error as:

$$e_1 = x_1 - x_{1d},\ e_2 = x_2 - V_{\text{ref}} \tag{20}$$

where x_{1d} denotes a virtual inductor current reference designed from the nominal current balance condition and augmented with a voltage-error damping term. At the desired nominal equilibrium, defined by $x_2 = V_{ref}$, $x_1 = x_{1d}$, $u = u_n$, and $\dot{x}_2 = 0$, the nominal output voltage dynamics yield the steady-state current-balance relation:

$$(1 - u_n)x_{1d} = \frac{V_{\text{ref}}}{R_n} + \frac{P_n}{V_{\text{ref}}} \tag{21}$$

The nominal duty ratio associated with the desired operating point is defined from the steady-state boost converter relation as:

$$u_n = 1 - \frac{V_{\text{in},n}}{V_{\text{ref}}} \tag{22}$$

Here, $u_n \in (0,1)$ denotes the nominal duty ratio corresponding to the desired operating point, which requires $V_{\text{ref}} > V_{\text{in},n}$.

Motivated by the current-balance relation in (21), the virtual inductor-current reference is selected as:

$$x_{1d} = \frac{1}{1-u_n}\left(\frac{V_{\text{ref}}}{R_n} + \frac{P_n}{V_{\text{ref}}} - k_v e_2\right), \qquad k_v > 0 \tag{23}$$

which recovers the nominal current-balance condition in (21) when $e_2 = 0$. Here, $k_v > 0$ represents a virtual damping conductance. The term $(-k_v e_2)$ modifies the virtual inductor-current reference in response to the output-voltage regulation error: a positive voltage error reduces the reference, whereas a negative voltage error increases it. This voltage-error feedback is introduced to counteract the destabilizing effect of the CPL's negative incremental conductance.

Define the duty-ratio deviation from the nominal operating point as:

$$\tilde{u} = u - u_n \tag{24}$$

Then, by separating an exact nominal passive core from the remaining dynamic coupling terms, the tracking-error dynamics can be written as:

$$\dot{e}_1 = -\frac{1-u_n}{L} e_2 + \frac{x_2}{L}\tilde{u} + \Delta_1 \tag{25}$$

$$\dot{e}_2 = \frac{1-u_n}{C} e_1 - \left(\frac{1}{R_n C} - \frac{P_n}{C\xi^2} + \frac{k_v}{C}\right) e_2 - \frac{x_{1d}}{C}\tilde{u} + \Delta_2 \tag{26}$$

For a constant voltage reference and a fixed nominal duty ratio, the residual terms in (25) and (26) are explicitly given by

$$\Delta_1 = d_1 - \dot{x}_{1d} = d_1 + \frac{k_v}{1-u_n}\dot{x}_2,\ \Delta_2 = d_2 - \frac{\tilde{u}e_1}{C}$$

These terms contain both the physical lumped disturbances and the dynamic coupling terms introduced by the chosen error-system decomposition. In particular, $\dot{x}_{1d}$ arises from the time-varying virtual current reference, whereas $-\frac{\tilde{u}e_1}{C}$ represents a bilinear state–input coupling.

The NESO estimates d_1 and d_2, rather than the complete residuals Δ_1 and Δ_2. To expose the nominal passive structure, the idealized passive core obtained by setting $\Delta_1 = \Delta_2 = 0$ is first analyzed. The remaining coupling and disturbance effects are retained in the subsequent regional closed-loop analysis.

The scalar ξ is the mean value theorem intermediate point between x_2 and V_{ref}, with $\xi > 0$ over the admissible voltage region. In particular,

$$\frac{P_n}{x_2} - \frac{P_n}{V_{\text{ref}}} = -\frac{P_n}{\xi^2}(x_2 - V_{\text{ref}}) = -\frac{P_n}{\xi^2} e_2 \tag{27}$$

This representation makes explicit the contribution of the CPL negative incremental conductance to the voltage error dynamics.

To characterize the nominal passive mapping, consider the energy-like storage function:

$$V_p = \frac{1}{2}Le_1^2 + \frac{1}{2}Ce_2^2 \tag{28}$$

The derivative of V_p along the error dynamics is:

$$\dot{V}_p = Le_1\dot{e}_1 + Ce_2\dot{e}_2 \tag{29}$$

Substituting (25) and (26) into (29) yields:

$$\dot{V}_p = -\left(\frac{1}{R_n} - \frac{P_n}{\xi^2} + k_v\right)e_2^2 + (x_2e_1 - x_{1d}e_2)\tilde{u} + Le_1\Delta_1 + Ce_2\Delta_2 \tag{30}$$

This motivates the definition of the passive output associated with the input ($\tilde{u}$) as:

$$y_p = x_2e_1 - x_{1d}e_2 \tag{31}$$

Consequently, in the presence of residual terms, the following bound holds:

$$\dot{V}_p \le -\left(\frac{1}{R_n} - \frac{P_n}{\xi^2} + k_v\right)e_2^2 + y_p\tilde{u} + L|e_1||\Delta_1| + C|e_2||\Delta_2| \tag{32}$$

In the idealized residual-free case, $\Delta_1 = \Delta_2 = 0$, one obtains:

$$\dot{V}_p \le -\alpha_v(\xi)e_2^2 + y_p\tilde{u} \tag{33}$$

where

$$\alpha_v(\xi) = \frac{1}{R_n} - \frac{P_n}{\xi^2} + k_v \tag{34}$$

Therefore, the mapping $\tilde{u} \mapsto y_p$ is passive with voltage-error dissipation over the admissible operating region whenever $\alpha_v(\xi) > 0$ for all admissible ξ.

This condition shows that the injected damping k_v must dominate the destabilizing CPL incremental conductance whenever P_n/ξ^2 exceeds the nominal resistive conductance $1/R_n$.

B. Explicit Connection with the CPL Incremental Conductance

As established in Section II under the adopted load-current convention, an ideal CPL described by $i_{\mathrm{CPL}} = P_n/v_o$ exhibits a negative local incremental conductance around an operating voltage.

$$g_{\mathrm{CPL,inc}} = \frac{\partial i_{\mathrm{CPL}}}{\partial v_o}\Big|_{v_o=V_o^*} = -\frac{P_n}{(V_o^*)^2} \tag{35}$$

Therefore, around the regulated operating point defined by $V_o^* = V_{\mathrm{ref}}$, the CPL contributes a negative incremental conductance in the output-voltage channel.

In the nonlinear error representation of Section III-A, the same destabilizing mechanism appears through the state dependent term $-P_n/\xi^2$, where ξ is the mean value theorem intermediate point between x_2 and V_{ref}. Unlike a small-signal linearization, this coefficient arises from the exact mean-value reformulation of the nonlinear CPL term over the admissible voltage region. Accordingly, the nonlinear error model suggests the following state-dependent effective incremental load conductance in the output-voltage channel:

$$g_{\mathrm{load,inc}}(\xi) = \frac{1}{R_n} - \frac{P_n}{\xi^2} \tag{36}$$

The damping injection introduced through the virtual current reference in (23) contributes the additional conductance-like term k_v in the voltage error dynamics. Therefore, the resulting voltage channel dissipation coefficient can be written as:

$$g_{\mathrm{eff}}(\xi) = g_{\mathrm{load,inc}}(\xi) + k_v = \frac{1}{R_n} - \frac{P_n}{\xi^2} + k_v \tag{37}$$

This is exactly the coefficient $\alpha_v(\xi)$ appearing in the storage function derivative in (33) and (34), thereby providing a direct interpretation of the passivity condition in conductance terms. Accordingly, positivity of the voltage-channel dissipation requires:

$$g_{\mathrm{eff}}(\xi) > 0, \frac{1}{R_n} - \frac{P_n}{\xi^2} + k_v > 0 \tag{38}$$

over the admissible voltage region of interest. When this condition is evaluated at the regulated equilibrium, where $x_2 = V_{\mathrm{ref}}$ and hence $\xi = V_{\mathrm{ref}}$, it reduces to:

$$\frac{1}{R_n} - \frac{P_n}{V_{\mathrm{ref}}^2} + k_v > 0 \tag{39}$$

Equivalently, to guarantee positive local dissipation at the regulated operating point, the damping gain should satisfy:

$$k_v > \frac{P_n}{V_{\mathrm{ref}}^2} - \frac{1}{R_n} \tag{40}$$

If the right-hand side is negative, then any choice $k_v > 0$ automatically satisfies this local damping requirement.

In the special case $k_v = 0$, the condition reduces to

$$\frac{1}{R_n} > \frac{P_n}{V_{\mathrm{ref}}^2} \tag{41}$$

or equivalently,

$$V_{\mathrm{ref}} > \sqrt{P_nR_n} \tag{42}$$

These inequalities should be interpreted as local operating-point design conditions derived from the conductance interpretation of the nonlinear passivity coefficient. Without damping injection, the resistive-load conductance must dominate the magnitude of the CPL negative incremental conductance at the regulated operating point. With $k_v > 0$, the injected conductance-like damping enlarges the admissible operating region by compensating for the CPL-induced loss of damping.

C. Nonlinear Extended State Observer

To estimate and compensate the lumped uncertainties acting in the inductor-current and output-voltage channels, two extended disturbance states are introduced and a measurement-driven dual-channel NESO is constructed. Using the nominal-plus-disturbance model introduced in (16), the perturbed boost-converter dynamics are written as:

$$\begin{cases} \dot{x}_1 = f_1(x,u) + d_1 \\ \dot{x}_2 = f_2(x,u) + d_2 \end{cases} \tag{43}$$

where

$$\begin{cases} f_1(x,u) = \frac{V_{in,n}}{L} - \frac{1-u}{L}x_2 \\ f_2(x,u) = \frac{1-u}{C}x_1 - \frac{x_2}{R_nC} - \frac{P_n}{Cx_2} \end{cases} \tag{44}$$

Here, d_1 and d_2 denote the lumped uncertainties entering the current and voltage channels, respectively. These

disturbances aggregate parameter mismatch, parasitic effects, CPL uncertainty, unmodeled losses, and other exogenous or neglected dynamics. The disturbance channels are modeled as:

$$\dot{d}_1 = h_1(t), \dot{d}_2 = h_2(t) \quad (45)$$

where $h_1(t)$ and $h_2(t)$ are assumed to be bounded disturbance-rate terms, i.e.,

$$|h_i(t)| < \bar{h}_i, \quad \text{i=1,2} \quad (46)$$

Accordingly, the following dual-channel NESO is employed to reconstruct the channel disturbances while generating auxiliary filtered state estimates:

$$\begin{cases} \dot{\hat{x}}_1 = f_1(x,u) + \hat{d}_1 - \beta_{11}\mathrm{fal}(\varepsilon_1) \\ \dot{\hat{x}}_2 = f_2(x,u) + \hat{d}_2 - \beta_{12}\mathrm{fal}(\varepsilon_2) \\ \dot{\hat{d}}_1 = -\beta_{21}\mathrm{fal}(\varepsilon_1) \\ \dot{\hat{d}}_2 = -\beta_{22}\mathrm{fal}(\varepsilon_2) \end{cases} \quad (47)$$

where the state estimation errors are defined as

$$\varepsilon_1 = \hat{x}_1 - x_1, \varepsilon_2 = \hat{x}_2 - x_2 \quad (48)$$

The positive constants $\beta_{11}, \beta_{12}, \beta_{21}, \beta_{22}$ are observer gains. The nonlinear correction function $\mathrm{fal}(\varepsilon_i)$ is defined as:

$$\mathrm{fal}(\varepsilon_i) = \begin{cases} \frac{\varepsilon_i}{\delta^{1-\alpha}}, & |\varepsilon_i| \le \delta \\ |\varepsilon_i|^{\alpha}\mathrm{sgn}(\varepsilon_i), & |\varepsilon_i| > \delta \end{cases} \quad (49)$$

Here, $0 < \alpha < 1$ and $\delta > 0$. The parameter α determines the nonlinear correction rate, while the strictly positive threshold δ specifies the width of the linear region around the origin. This condition ensures that the coefficient $c_\delta = \delta^{\alpha-1}$, used in the observer-error decomposition and Lyapunov analysis, is finite and well defined.

Although x_1 and x_2 are measurable in practice, the observer generates the auxiliary estimates $\hat{x}_1$ and $\hat{x}_2$ together with the disturbance estimates $\hat{d}_1$ and $\hat{d}_2$. This structure provides a unified mechanism for state-error filtering and dual-channel disturbance reconstruction. Moreover, the nonlinear $\mathrm{fal}(\varepsilon_i)$ correction treats small and large estimation errors differently. The observer gains should be selected by balancing convergence speed against sensitivity to measurement noise and unmodeled high-frequency dynamics.

For observer error analysis, the disturbance-estimation errors are additionally defined as:

$$\eta_1 = \hat{d}_1 - d_1, \eta_2 = \hat{d}_2 - d_2 \quad (50)$$

Using the plant and observer dynamics, the channel wise observer error equations are obtained as:

$$\begin{cases} \dot{\varepsilon}_1 = \eta_1 - \beta_{11}\mathrm{fal}(\varepsilon_1) \\ \dot{\eta}_1 = -\beta_{21}\mathrm{fal}(\varepsilon_1) - h_1(t) \\ \dot{\varepsilon}_2 = \eta_2 - \beta_{12}\mathrm{fal}(\varepsilon_2) \\ \dot{\eta}_2 = -\beta_{22}\mathrm{fal}(\varepsilon_2) - h_2(t) \end{cases} \quad (51)$$

For compact notation, β_{1i} and β_{2i} denote the state error and disturbance error injection gains of the i-th channel, respectively; that is, (β_{11}, β_{21}) for i=1 and (β_{12}, β_{22}) for i=2. By defining the overall observer-error vector as:

$$\theta = [\varepsilon_1 \quad \eta_1 \quad \varepsilon_2 \quad \eta_2]^T \quad (52)$$

the observer-error dynamics can be compactly written in nonlinear perturbed form as:

$$\dot{\theta} = F(\theta) + H(t) \quad (53)$$

where

$$H(t) = [0 \quad -h_1(t) \quad 0 \quad -h_2(t)]^T \quad (54)$$

Since $h_1(t)$ and $h_2(t)$ are bounded, the observer-error system is driven by bounded disturbance rate inputs. In the linear region of the $\mathrm{fal}(\varepsilon_i)$ function, i.e., for $|\varepsilon_i| \le \delta$, each observer-error channel can be represented as:

$$\begin{bmatrix} \dot{\varepsilon}_i \\ \dot{\eta}_i \end{bmatrix} = A_{oi}\begin{bmatrix} \varepsilon_i \\ \eta_i \end{bmatrix} + \begin{bmatrix} 0 \\ -h_i(t) \end{bmatrix}, \quad \text{i=1,2} \quad (55)$$

where

$$A_{oi} = \begin{bmatrix} -\frac{\beta_{1i}}{\delta^{1-\alpha}} & 1 \\ -\frac{\beta_{2i}}{\delta^{1-\alpha}} & 0 \end{bmatrix} \quad (56)$$

The characteristic polynomial of A_{oi} is

$$s^2 + \frac{\beta_{1i}}{\delta^{1-\alpha}}s + \frac{\beta_{2i}}{\delta^{1-\alpha}} \quad (57)$$

The characteristic polynomial in (57) is Hurwitz for positive observer gains. Hence, $A_o = diag(A_{o1}, A_{o2})$ is Hurwitz. To express the nonlinear observer-error dynamics exactly, define:

$$r_i(\varepsilon_i) = \mathrm{fal}(\varepsilon_i) - c_\delta\varepsilon_i, c_\delta = \delta^{\alpha-1}, i = 1,2$$

The residual r_i vanishes identically for $|\varepsilon_i| \le \delta$. Using this definition, (51) can be written as:

$$\dot{\theta} = A_o\theta + \Psi_o(\theta, t)$$

where Ψ_o contains the nonlinear residual terms and the disturbance-rate inputs, as specified in Appendix A.

Under the disturbance-rate bounds in (46) and known uniform residual bounds

$$|r_i(\varepsilon_i(t))| \le \bar{r}_i, i = 1,2$$

along the trajectories under consideration, Appendix A establishes the following inequality for the observer-error dynamics:

$$\dot{V}_o \le -\lambda_o\|\theta\|^2 + \sigma_o \quad (58)$$

Here, $\lambda_o > 0$ and $\sigma_o \ge 0$. The Lyapunov function is defined as:

$$V_o = \theta^T P_o\theta, P_o = P_o^T > 0 \quad (59)$$

where P_o is the unique symmetric positive-definite solution of:

$$A_o{}^T P_o + P_o A_o = -Q_o$$

for a selected $Q_o = Q_o{}^T > 0$. Explicit admissible constants are

$$\lambda_o = \frac{\lambda_{min}(Q_o)}{2}, \sigma_o = \frac{2\|P_o\|_2^2}{\lambda_{min}(Q_o)}\sum_{i=1}^{2}\left[\beta_{1i}{}^2\bar{r}_i{}^2 + \left(\beta_{2i}\bar{r}_i + \bar{h}_i\right)^2\right]$$

In the linear region of $fal(\varepsilon_i)$, the residual contribution is zero. Appendix A provides the derivation, a closed-form construction of P_o, regional residual bounds, and a sufficient invariance condition.

Consequently, the estimated disturbance vector

$$\hat{d} = [\hat{d}_1 \quad \hat{d}_2]^T \quad (60)$$

provides online estimates of the lumped uncertainties acting in the current and voltage channels, respectively.

D. Composite PBC+NESO Control Law

The composite control input is constructed from the nominal duty ratio, a passive-output damping term, and a NESO-based disturbance-compensation term. Since the control input is the boost-converter duty ratio, the implemented signal is constrained through saturation as:

$$u = sat_{[u_{min}.u_{max}]}\left(u_n - k_p y_p + u_c\right) \quad (61)$$

where u_n is the nominal duty ratio defined in (22), y_p is the passive output defined in (31), $k_p > 0$ is the passive-output damping gain, and u_c is the NESO-based disturbance compensation term.

The term u_n sets the nominal operating duty ratio, while the passive-output feedback term $-k_p y_p$ injects additional damping into the nominal passive error dynamics. The compensation term u_c is designed to attenuate the dominant lumped uncertainty entering the output-voltage channel. From the nominal-plus-disturbance voltage dynamics used for observer and controller design:

$$\dot{x_2} = \frac{(1-u)x_1}{C} - \frac{x_2}{CR_n} - \frac{P_n}{Cx_2} + d_2 \quad (62)$$

the compensation term u_c enters the voltage dynamics through the channel $-x_1 u_c/C$. To compensate for the estimated voltage-channel disturbance through this input channel, we impose the approximate cancellation condition:

$$-\frac{x_1}{C}u_c + \hat{d}_2 \approx 0 \quad (63)$$

This leads to the implementable compensation law:

$$u_c = \frac{C}{\hat{x}_{1\varepsilon}}\hat{d}_2 \quad (64)$$

where the regularized inductor-current-estimate is defined by:

$$\hat{x}_{1\varepsilon} = max\{\hat{x}_1, \varepsilon_u\}, \quad \varepsilon_u > 0 \quad (65)$$

where $\varepsilon_u > 0$ is a prescribed regularization threshold, with the same units as the inductor current, that keeps the denominator in (64) bounded away from zero. The regularized estimate $\hat{x}_{1\varepsilon}$ prevents a numerical singularity in the compensation gain when the estimated inductor current approaches zero. Under normal continuous-conduction mode operation of the boost converter, the inductor current is expected to remain positive; nevertheless, this regularization guarantees numerical robustness during startup and large transient phases.

To analyze the implemented saturated control law, consider the storage function V_p defined in (28). Define the unsaturated duty-ratio command and the saturation mismatch as:

$$q = u_n - k_p y_p + u_c,\ s_u = sat_{[u_{min},u_{max}]}(q) - q$$

The implemented duty-ratio deviation therefore satisfies the exact identity $\tilde{u} = -k_p y_p + u_c + s_u$

Substitution into the plant-side storage inequality (32) gives

$$\dot{V_p} \le -\alpha_v(\xi)e_2^2 - k_p y_p^2 + y_p u_c + y_p s_u + |e_1|L|\Delta_1| + |e_2|C|\Delta_2| \quad (66)$$

This expression applies to the saturated implementation; the unsaturated case is recovered by setting $s_u = 0$. Here, $\alpha_v(\xi) = \frac{1}{R_n} - \frac{P_n}{\xi^2} + k_v$, as defined in (34). The gains k_v and k_p have distinct but complementary roles. The gain k_v, introduced through the virtual current reference (23), shapes the nominal voltage-channel dissipation coefficient. For the regional analysis, this coefficient must have a uniform positive lower bound throughout the operating region; the local condition (40), evaluated at the regulated equilibrium, does not by itself establish this regional requirement. In contrast, $k_p > 0$ supplies passive-output damping through the term $-k_p {y_p}^2$ in (66). The regional closed-loop analysis combines these two dissipation contributions while explicitly retaining compensation, virtual-reference coupling, and saturation effects. The joint contribution of these two dissipation terms is quantified by the positive-definite matrix estimate in Appendix B, equation (B.4), under the stated regional assumptions.

Using the compensation law (64) and the regularized estimate (65), define the voltage-channel compensation residual as

$$r_c = d_2 - \frac{x_1}{C}u_c = d_2 - \frac{x_1}{\hat{x}_{1\varepsilon}}\hat{d}_2 \quad (67)$$

Since $\eta_2 = \hat{d}_2 - d_2$, this identity becomes

$$r_c = -\eta_2 + \left(1 - \frac{x_1}{\hat{x}_{1\varepsilon}}\right)\hat{d}_2$$

Thus, the residual depends on both the disturbance-estimation error and the regularized current-estimation mismatch. If

$$|d_2| \le \bar{d}_2,\ \left|1 - \frac{x_1}{\hat{x}_{1\varepsilon}}\right| \le \bar{\chi}$$

then

$$|r_c| \le \bar{\chi}\bar{d}_2 + (1+\bar{\chi})\|\theta\|$$

Including saturation, the corresponding voltage-channel residual is

$$r_{c,s} = r_c - \frac{x_1}{C}s_u$$

Hence, on a region where $|x_1| \le \bar{\chi}_1$ and $|s_u| \le \bar{s}_u$

$$\left|r_{c,s}\right| \le \bar{\chi}\bar{d}_2 + (1+\bar{\chi})\|\theta\| + \frac{\bar{\chi}_1}{C}\bar{s}_u$$

These residual expressions clarify the compensation mechanism. The regional closed-loop analysis in Section III-E proceeds directly from (66), without adding a separate $r_{c,s}$ contribution to the same storage inequality, thereby avoiding double counting.

E. Closed-Loop Stability and Ultimate Boundedness

We now state the main closed-loop boundedness result for the proposed composite PBC+NESO controller.

Assumption 1. The reference V_{ref} is constant on the interval considered. The plant operates in a prescribed compact region

$$R_x = x: |x_1| \le \bar{X}_1, \underline{v} \le x_2 \le \bar{X}_2,\ 0 < \underline{v} \le V_{ref} \le \bar{X}_2$$

where $\bar{X}_1 > 0$ is the prescribed current-magnitude limit, and $\underline{v}$ and $\bar{X}_2$ are the prescribed lower and upper voltage limits. On the interval considered, the plant trajectory remains in R_x.

The lumped disturbances d_i, i=1,2, are locally absolutely continuous along the trajectories and satisfy

$|d_i(t)| \le \bar{d}_i$, $|\dot{d}_i(t)| \le \bar{h}_i$

almost everywhere, Here, $\bar{d}_i > 0$ and $\bar{h}_i > 0$ are finite, uniform bounds on the disturbance magnitudes and their total time derivatives along the trajectories, respectively; these bounds are independent of the initial time. The implemented duty ratio satisfies

$u(t) \in [u_{min}, u_{max}],\ 0 \le u_{min} \le u_{max} \le 1$

where u_{min} and u_{max} are the actuator saturation limits.

Assumption 2. The controller gains satisfy, $k_p > 0$, $k_v > 0$ and $\alpha_v(\xi) \ge \alpha_0 > 0$ throughout the operating region, where α_0 is a uniform positive lower bound. The observer gains are positive, $0 < \alpha < 1$, $\delta > 0$.

For the observer state-estimation errors $\varepsilon_i = \hat{x}_i - x_i$, define the nonlinear residuals: $r_i(\varepsilon_i) = fal(\varepsilon_i) - \delta^{\alpha-1}\varepsilon_i$

satisfy known uniform bounds: $|r_i(\varepsilon_i(t))| \le \bar{r}_i$, $i = 1,2$

over the interval considered, where $\bar{r}_i \ge 0$ are finite, uniform residual bounds independent of the initial time. Appendix A gives explicit expressions for these bounds on a prescribed observer-error region and derives the corresponding observer Lyapunov estimate.

The following result applies while these regional conditions hold. Appendix B provides a sufficient condition for their continued validity.

For the subsequent composite analysis, the observer-error dynamics recalled from Section III-C are represented in the compact form:

$$\dot{\theta} = A_o\theta + \Psi_o(\theta, t) \tag{68}$$

where $\theta = [\varepsilon_1 \quad \eta_1 \quad \varepsilon_2 \quad \eta_2]^T$ is the observer-error vector defined in (52), and $A_o = diag(A_{o1}, A_{o2})$ is assembled from the matrices in (56). With the residual definition introduced in Section III-C:

$$\Psi_o(\theta, t) = \begin{bmatrix} -\beta_{11} r_1(\varepsilon_1) \\ -\beta_{21} r_1(\varepsilon_1) - h_1(t) \\ -\beta_{12} r_2(\varepsilon_2) \\ -\beta_{22} r_2(\varepsilon_2) - h_2(t) \end{bmatrix}$$

Thus, (68) is an exact decomposition of the nonlinear observer-error dynamics. Its bounded-input estimate uses the disturbance-rate bounds in Assumption 1 and the residual bounds in Assumption 2.

Proposition 1. Under Assumptions 1 and 2, consider the composite Lyapunov function:

$$V_c = V_p + \rho V_o \tag{69}$$

where V_p and V_o are defined in (28) and (59), respectively, and $\rho > 0$ is an analysis weight. With the explicit regional constants $c_0 > 0$ and $c_1,\ c_2 \ge 0$ defined in Appendix B, select $\rho > \frac{c_1^2}{c_0 \lambda_o}$

Where $\lambda_o > 0$ and $\sigma_o \ge 0$ are the observer-estimate constants specified following (58). Then, while the regional conditions hold,

$$\dot{V}_c \le -\lambda_e \|e\|^2 - \lambda_\theta \|\theta\|^2 + \bar{\delta}, \quad \text{e} = [e_1 \quad e_2]^T \tag{70}$$

where θ is the observer-error vector in (68) and $\lambda_e = \frac{c_0}{2}$, $\lambda_\theta = \rho\lambda_o - \frac{c_1^2}{c_0} > 0$, $\bar{\delta} = \frac{c_2^2}{c_0} + \rho\sigma_o$

Here, $\bar{\delta} \ge 0$ is the composite residual constant, distinct from the observer threshold δ.

Define: $m_e = \frac{minL,C}{2}$, $M_e = \frac{maxL,C}{2}$, $p_{min} = \lambda_{min}(P_o) > 0$, $p_{max} = \lambda_{max}(P_o)$

denote the minimum and maximum eigenvalues of P_o. Set:

$k = min\frac{\lambda_e}{M_e}, \frac{\lambda_\theta}{\rho p_{max}} > 0$

Then, for $t \ge t_0$ within that interval:

$$V_c(t) \le V_c(t_0)e^{-k(t-t_0)} + \frac{\bar{\delta}}{k}\left(1 - e^{-k(t-t_0)}\right) \tag{71a}$$

Then:

$$\lim_{t\to\infty} sup\ \|e(t)\| \le \sqrt{\frac{\bar{\delta}}{k m_e}}$$

$$\lim_{t\to\infty} sup\ \|\theta(t)\| \le \sqrt{\frac{\bar{\delta}}{k\rho p_{min}}} \tag{71b}$$

$$\lim_{t\to\infty} sup\ |x_2(t) - V_{ref}| \le \sqrt{\frac{2\bar{\delta}}{kC}}$$

Under this continued-validity condition, any strictly larger bounds are attained and maintained after a finite time, uniformly over bounded initial-error sets sharing the same regional constants and analysis weight.

Proof: Appendix B derives (70) from the saturated plant-storage inequality (66) and the observer estimate (58). The quadratic bounds

$m_e\|e\|^2 + \rho p_{min}\|\theta\|^2 \le V_c \le M_e\|e\|^2 + \rho p_{max}\|\theta\|^2$

and the definition of k imply: $\dot{V}_c \le -kV_c + \bar{\delta}$

The comparison principle gives (71a). The lower quadratic bounds, together with $V_c \ge \frac{Ce_2^2}{2}$ and $e_2 = x_2 - V_{ref}$, yield (71b). The exponentially decaying term in (71a) establishes the stated finite-time entry into any strictly larger bounds. The certified bounds depend on the controller gains through c_0, c_1, c_2 and on the observer gains through P_o, λ_o, σ_o.

III. Simulation Results and Performance Evaluation

To evaluate the effectiveness of the proposed control strategy, simulations are carried out in the MATLAB/Simulink environment for the considered DC–DC boost converter supplying a parallel resistive load and a constant power load (CPL). The baseline operating conditions are $V_{in} = 15\ V$, $V_{ref} = 30\ V$, a parallel resistance of $60\ \Omega$ and a nominal CPL power of $32.14\ W$. These quantities are varied where specified in the individual scenarios. The proposed controller is implemented using the composite PBC+NESO structure shown in Fig. 3, where the measured output voltage v_o and inductor current i_L are fed back to the passivity-based controller and the observer. The NESO estimates the lumped disturbances and generates a compensation signal, which is superimposed on the nominal

passivity-based control action prior to the duty-ratio saturation. The main circuit and simulation parameters are summarized in Table 1.

Table 1. System Parameters Used in the Simulations

Parameter	Symbol	Value
Baseline Input voltage	$V_{in,0}$	15 V
Baseline Output voltage reference	$V_{ref,0}$	30 V
Inductor	L	0.3 mH
Output capacitor	C	1000 μF
Switching frequency	f_s	20 kHz
Baseline parallel-load resistance	R_0	60 Ω
Nominal CPL power	$P_{CPL,0}$	32.14 W
Buck-converter output-voltage reference	$V_{buck,ref}$	15 V
Baseline buck-converter load resistance	$R_{buck,0}$	7 Ω

In the simulation model, the CPL branch is realized by a voltage-regulated buck converter with ideal switching and passive components. At the baseline regulated operating point, its nominal lossless input power is $P_{CPL,0} = \frac{V_{buck,ref}{}^2}{R_{buck,0}} = \frac{15^2}{7} \approx 32.14\,W$. This is a nominal steady state value: the buck converter retains its internal dynamics during transients, whereas the analytical model uses the ideal CPL approximation. The buck-converter voltage-controller settings are identical for all compared upstream control architectures.

For a comparative performance assessment, four control schemes are considered: dual-loop PI, standalone passivity-based control (PBC-only), PBC combined with an extended nonlinear disturbance observer adopted from [22] (PBC+ENDO), and the proposed PBC with a nonlinear extended state observer (PBC+NESO). Table 2 presents the controller and observer parameters grouped by control architecture and functional component. The voltage- and current-loop PI gains are listed separately. For the observer-assisted PBC schemes, the PBC parameters are distinguished from the observer parameters: λ_1 and λ_2 belong to ENDO, whereas β_{11}, β_{12}, β_{21}, β_{22}, α and δ belong to NESO. For each control scheme, the controller and observer parameters are kept unchanged across the simulation scenarios.

Table 2. Controller and observer parameters used in the simulations

Control scheme	Component / loop	Symbol	Value
PI	Voltage loop	K_{pv}	1
	Voltage loop	K_{iv}	100
	Current loop	K_{pi}	0.5
	Current loop	K_{ii}	0.1
PBC-only	Passive-output feedback	k_p	0.82
	Voltage-channel damping	k_v	1
PBC+ENDO	ENDO: current channel	λ_1	600
	ENDO: voltage channel	λ_2	1000
	Passive-output feedback	k_p	0.82
	Voltage-channel damping	k_v	1
PBC+NESO	NESO	β_{11}	2450
	NESO	β_{12}	2450
	NESO	β_{21}	1.225×10^7
	NESO	β_{22}	1.225×10^7
	NESO	α	0.8
	NESO	δ	0.1
	Passive-output feedback	k_p	0.82
	Voltage-channel damping	k_v	1

In the PI gain notation, the subscripts v and i identify the voltage and current loops, respectively. The gains K_{pv} and K_{iv} belong to the voltage loop, whereas K_{pi} and K_{ii} belong to the current loop. For ENDO, λ_1 and λ_2 are the observer gains of the inductor-current and output-voltage channels, respectively; for NESO, β_{11}, β_{12} are the state-estimation error-injection gains, whereas β_{21}, β_{22} are the disturbance-estimation error-injection gains. The parameters α and δ define the nonlinear correction function in Eq. (49).

Parameter selection and comparison protocol

PI tuning. Preliminary nominal-point small-signal considerations were used to guide the initial PI gain range. The final gains were then selected through manual MATLAB/Simulink tuning, first for the inner current loop and subsequently for the outer voltage loop, with refinement using all four reported scenarios. The assessment considered sustained oscillations, peak positive voltage deviations, settling time, steady-state tracking error, and integral voltage-error indices. The 1% band was used to define settling time. The resulting gains are $K_{pv} = 1$, $K_{iv} = 100$, $K_{pi} = 0.5$, $K_{ii} = 0.1$.

PBC gains. The three PBC-based architectures use the same gains, $k_p = 0.82$ and $k_v = 1$. Their selection combined the theoretical sign/dissipation requirements with manual transient-response assessment. In particular, Eq. (40) provides the local voltage-channel damping requirement

$$k_v > \frac{P_n}{V_{\mathrm{ref}}^2} - \frac{1}{R_n}$$

Whereas $k_p > 0$ determines the passive-output feedback contribution. These conditions guide admissible choices but do not uniquely determine the numerical gains.

ENDO gains. The implemented ENDO uses the auxiliary-state disturbance-observer structure adopted from [22], with the nominal converter functions defined in (44). The observer gains $\lambda_1 = 600$ and $\lambda_2 = 1000$ were selected by manual assessment of the closed-loop responses under the reported scenarios. These values are specific to the present implementation and are not copied from the reference. The comparison concerns this implemented baseline rather than an exact reproduction of the reference's complete controller.

NESO gains. The NESO injection gains were selected using the frequency-scaled parameterization

$\beta_{11} = \beta_{12} = k_1\omega_0, \beta_{21} = \beta_{22} = k_2{\omega_0}^2$

together with manual response-based refinement. The selected values $\omega_0 = 3500$, $k_1 = 0.7$, and $k_2 = 1$ give

$\beta_{11} = \beta_{12} = 2450, \beta_{21} = \beta_{22} = 1.225 \times 10^7$

with $\alpha = 0.8$ and $\delta = 0.1$. Specifically, in the linear region of the nonlinear correction function, Eq. (57) gives:

$p_i(s) = s^2 + ck_1\omega_0 s + ck_2{\omega_0}^2, c = \delta^{\alpha-1}$

Thus, ω_0 is a tuning frequency scale rather than an asserted exact bandwidth of the nonlinear observer. Positive injection gains make the local homogeneous error matrix Hurwitz; the regional nonlinear and closed-loop conclusions remain subject to the assumptions stated in Section III and Appendix A.

Common test conditions and interpretation. All control architectures were evaluated using the same converter/load models, disturbance profiles, initial conditions, solver and time-step settings, measurement/filtering arrangements, and actuator constraints. The downstream buck-converter voltage-control settings were also kept unchanged. Following tuning, one fixed parameter set per architecture was used across all four scenarios, without scenario-specific retuning. The shared PBC gains provide a common-core comparison, not independently optimal tuning of each complete PBC architecture. Moreover, the reported scenarios also informed manual tuning and therefore do not constitute an independent held-out validation set. The results should consequently be interpreted as comparisons of the reported implementations under common test conditions.

ENDO benchmark implementation and comparison with NESO

The PBC+ENDO benchmark employs the auxiliary-state disturbance observer adopted from [22]. Using the nominal-plus-disturbance model in (43)-(44), its implementation is given by

$$\begin{cases} \hat{d}_i = z_{di} + \lambda_i x_i \\ \dot{z}_{di} = -\lambda_i[z_{di} + \lambda_i x_i + f_i(x,u)] \end{cases} \quad \text{i=1,2}$$

Where $x_1 = i_L, x_2 = v_o, z_{di}$ denotes the internal auxiliary state, and $\lambda_i > 0$ is the observer gain for the corresponding channel. The nominal functions $f_i(x,u)$ are those defined in (44). The implemented gains are $\lambda_1 = 600$ and $\lambda_2 = 1000$, corresponding to the current and voltage channels, respectively. This realization reconstructs the disturbance estimates without requiring numerical differentiation of the measured states.

For the disturbance-estimation error $\tilde{d}_i = \hat{d}_i - d_i$, the ideal error dynamics satisfy:

$\dot{\tilde{d}}_i = -\lambda_i\tilde{d}_i - \dot{d}_i$

Thus, constant disturbances yield exponential convergence, while differentiable disturbances satisfying $|\dot{d}_i| \le \bar{h}_i$ yield

$$\limsup_{t\to\infty} |\tilde{d}_i(t)| \le \frac{\bar{h}_i}{\lambda_i}$$

These statements assume the stated model and ideal measurements; discontinuous disturbance changes must be treated separately at their jump instants.

Structurally, the ENDO contains one auxiliary state per channel and reconstructs each disturbance estimate as $z_{di} + \lambda_i x_i$, without introducing separate state-estimation dynamics. In contrast, the NESO in (47)-(49) maintains both a state estimate and a disturbance estimate in each channel. Its correction terms are driven by the state-estimation error through the nonlinear fal function, with separate injection gains β_{1i} and β_{2i}. Consequently, the implemented ENDO has two internal observer states, whereas the NESO has four. Both observers use the measured inductor current and output voltage.

The fal correction is linear within its boundary region and grows sublinearly outside it. This distinguishes the NESO correction mechanism from the fixed-gain first-order disturbance-error dynamics of the ENDO.

As discussed in Sections II and III, a constant power load exhibits a negative incremental impedance characteristic, which reduces the effective damping of the converter and can intensify transient voltage oscillations. Therefore, evaluating the control performance under CPL operation is particularly important in DC microgrid applications. In the following, the simulation results are presented to examine the voltage regulation capability, transient response quality, and disturbance rejection performance of the considered control schemes.

Scenario 1: Performance Under Step Variations of the CPL

The CPL power increases from 32.14 W to 62.14 W at t=0.05 s and returns to 32.14 W at t=0.15 s, while the output-voltage reference remains at 30 V. Figures 4 and 5 show the output-voltage and inductor-current responses, respectively. Tables 3 and 4 quantify voltage-regulation performance, while Fig. 5 illustrates the associated current dynamics.

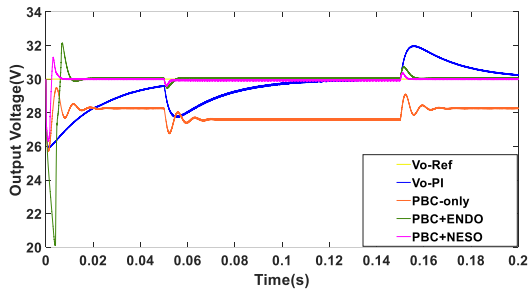


Fig. 4. Output voltage response under step load variations in Scenario 1.

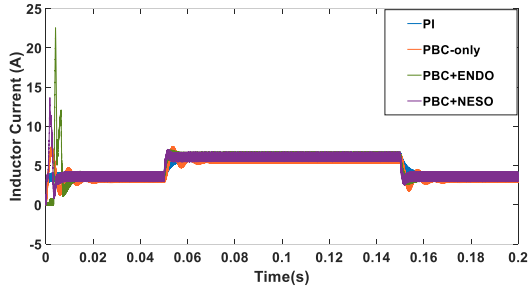


Fig. 5. Inductor current response under step load variations in Scenario 1.

In Tables 3, 5, 7, and 9, PD denotes the peak positive output-voltage deviation above the reference (percentage overshoot) within each evaluation interval, expressed as a percentage of the corresponding reference voltage; settling time (Ts) is the elapsed time after each load transition required to enter and remain within the ±1% reference band for the remainder of that interval; and mean absolute error (MAE) is the average absolute voltage error over the corresponding interval. Subscripts 1 and 2 denote the intervals 0.05-0.15 s and 0.15-0.20 s, respectively. N/A indicates that the settling criterion is not met within the corresponding interval. PD measures overshoot only and does not quantify voltage undershoot; therefore, zero PD does not imply zero tracking error or satisfaction of the settling criterion.

Table 3. Output-Voltage Performance Metrics in Scenario 1

Metric	PI	PBC-only	PBC+ENDO	PBC+NESO
First interval 0.05 to 0.15				
PD1 (%)	7.61	10.8	1.77	1.44
Ts1 (ms)	51.96	N/A	3.07	1.87
MAE1 (V)	0.9408	1.7408	0.0422	0.0129
Second interval 0.15 to 0.2				
PD2 (%)	6.6	2.96	2.46	1.27
Ts2 (ms)	47.08	N/A	4.24	1.60
MAE2 (V)	0.4126	1.7399	0.0419	0.0128

Table 3 reports lower percentage overshoots and shorter settling times for the observer-assisted controllers than for PI. Following the load increase and decrease, PBC+NESO achieves percentage overshoots of 1.44% and 1.27%, compared with 1.77% and 2.46% for PBC+ENDO. Its corresponding settling times are 1.87 and 1.60 ms, versus 3.07 and 4.24 ms for PBC+ENDO and 51.96 and 47.08 ms for PI.

PBC-only does not satisfy the 1% settling criterion in either interval; PBC+NESO also achieves the lowest MAEs, at 0.0129 and 0.0128 V, respectively. Table 4 summarizes the integral voltage-error indices.

Table 4. Integral Voltage Error Indices in Scenario 1

Metric	PI	PBC-only	PBC+ENDO	PBC+NESO
IAE	0.13418	0.37933	0.011047	0.0082508
ITAE	0.012959	0.040972	0.0012395	0.00085433
ISE	0.17018	0.82346	0.0021323	0.00079756
ITSE	0.015613	0.087432	0.00025912	7.9751×10^{-5}

In Table 4, IAE and ISE integrate the absolute and squared voltage errors, respectively, while ITAE and ITSE additionally weight these errors by time. PBC+NESO yields the lowest reported values of all four indices. Overall, the reported results indicate faster voltage recovery and lower accumulated voltage error with PBC+NESO under the tested CPL variations.

Scenario 2: Performance Under Step Reference-Voltage Variations

The output-voltage reference is initially set to 24 V and increased to 36 V at t=0.1 s to evaluate reference tracking under CPL conditions. Figures 6 and 7 show the output-voltage and inductor-current responses, respectively. The quantitative assessment focuses on voltage tracking, while Fig. 7 illustrates the associated current dynamics.

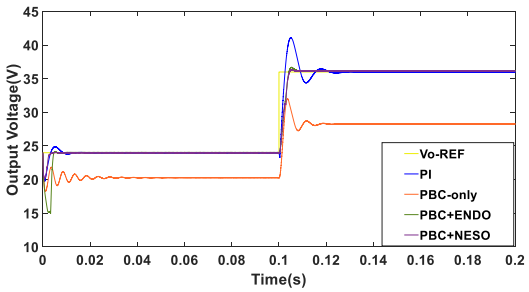


Fig. 6. Output-voltage response under reference-voltage variations in Scenario 2.

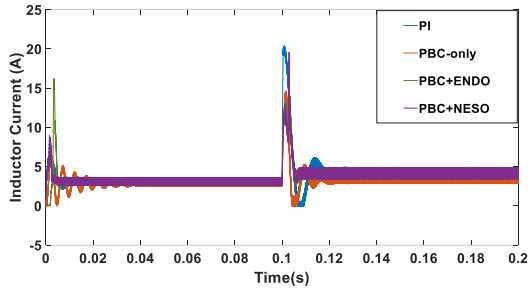


Fig. 7. Inductor-current response under reference-voltage variations in Scenario 2.

Table 5 compares performance in the two reference-voltage intervals using the 1% settling criterion and the MAE definition introduced in Scenario 1. At 24 V and 36 V, respectively, PBC+NESO achieves settling times of 3.1125 and 5.489 ms, compared with 4.5675 and 6.8375 ms for PBC+ENDO and 7.742 and 19.235 ms for PI. PBC-only does not meet the settling criterion in either interval and has MAEs of 3.7160 and 7.7632 V. PBC+NESO has the lowest reported MAE in both intervals, at 0.07554 and 0.41918 V. Among the controllers satisfying the settling criterion, PBC+NESO also yields the lowest reported PD in both intervals, at 0.2116% and 1.0352%, compared with 0.7099% and 1.9454% for PBC+ENDO.

Table 5. Output Voltage Performance Metrics in Scenario 2

Performance Metric	PI	PBC-only	PBC+ ENDO	PBC+ NESO
First interval: V_{ref}=24 V				
Ts1(ms)	7.742	N/A	4.5675	3.1125
PD1 (%)	3.7289	1.24×10^{-5}	0.7099	0.2116
MAE1 (V)	0.11827	3.7160	0.30510	0.07554
Second interval: V_{ref}=36 V				
Ts2(ms)	19.235	N/A	6.8375	5.489
PD2 (%)	14.1929	0	1.9454	1.0352
MAE2 (V)	0.47325	7.7632	0.43969	0.41918

Table 6 presents the integral voltage-error indices defined in Scenario 1.

Table 6. Integral Voltage Error Indices in Scenario 2

Integral Error Index	PI	PBC-only	PBC+ENDO	PBC+NESO
IAE	0.059144	1.147915	0.074471	0.049464
ITAE	0.0051201	0.134863	0.0055538	0.0050848
ISE	0.27900	7.51616	0.42695	0.24804
ITSE	0.025996	0.98045	0.023456	0.023278

PBC+NESO yields the lowest IAE, ITAE, ISE, and ITSE values in Table 6. However, its reductions in ITAE relative to PI and in ITSE relative to PBC+ENDO are modest, approximately 0.69% and 0.76%, respectively. Overall, PBC+NESO achieves the shortest 1% settling times and the lowest reported mean absolute and integral voltage errors under the tested reference-voltage conditions.

Scenario 3: Parallel Resistive Load Variation in the Presence of CPL

The reference voltage is maintained at 30 V, while the resistive load connected in parallel with the CPL changes from 60 Ω to 15 Ω at t=0.05 s and returns to 60 Ω at t=0.15 s. Figs. 8 and 9 show the corresponding output-voltage and inductor-current responses, respectively.

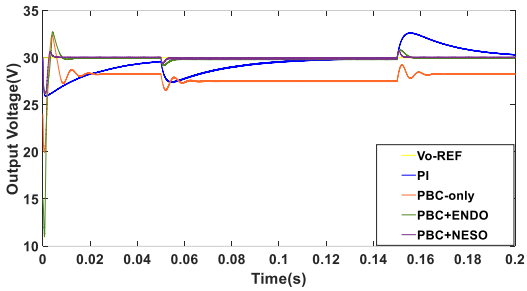


Fig. 8. Output-voltage responses under parallel resistive load variations (60 Ω ↔ 15 Ω) in the presence of CPL in Scenario 3

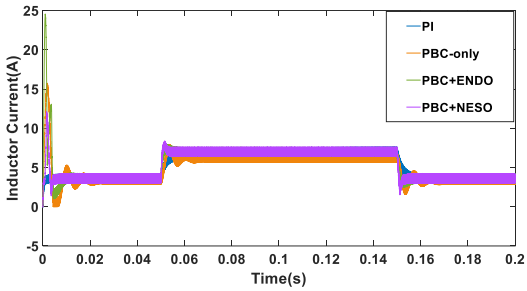


Fig. 9. Inductor-current responses under parallel resistive load variations (60 Ω ↔ 15 Ω) in the presence of CPL in Scenario 3

Table 7 compares the responses to both load changes using the performance metrics defined in Scenario 1. PBC+NESO achieves the shortest settling times under the ±1% criterion, at 1.9675 and 1.7935 ms, compared with 4.8665 and 4.0955 ms for PBC+ENDO. PI settles in 64.211 ms after the first change but does not meet the settling criterion within the second evaluation interval. PBC-only does not meet this criterion within either evaluation interval. PBC+NESO also yields the lowest reported PD and MAE values for both load changes.

TABLE 7. Output-Voltage Performance Metrics for Scenario 3

Metric	PI	PBC-only	PBC+ENDO	PBC+NESO
Ts1 (ms)	64.211	N/A	4.8665	1.9675
PD1 (%)	8.7583	11.5815	2.8250	2.1027
MAE1 (V)	0.7627	2.5065	0.1794	0.0832
Ts2 (ms)	N/A	N/A	4.0955	1.7935
PD2 (%)	8.8273	8.3790	2.7498	2.4693
MAE2 (V)	1.2541	1.7146	0.0638	0.0547

TABLE 8. Integral Voltage Error Indices for Scenario 3

Index	PI	PBC-only	PBC+ENDO	PBC+NESO
IAE	0.13898	0.33638	0.02113	0.01106
ITAE	0.009218	0.02322	0.001149	0.000696
ISE	0.22097	0.77943	0.005625	0.001656
ITSE	0.01370	0.04982	0.0002915	0.0000947

Note: These indices were calculated from t = 0.05 s to the end of the simulation interval.

Table 8 presents the integral voltage-error indices evaluated from t=0.05 s to the end of the simulation. PBC+NESO has the lowest reported values across all four indices: IAE, ITAE, ISE, and ITSE. Together, these results indicate faster output-voltage recovery and lower voltage errors for PBC+NESO than for the other tested controllers under the considered parallel resistive-load variations.

Scenario 4: Robustness Evaluation Under Input Voltage Variations in the Presence of CPL

The output-voltage reference is maintained at 30 V with a CPL and a parallel 60 Ω resistive load. The input voltage changes from 15 to 12 V at t=0.05 s, increases to 18 V at t=0.10 s, and returns to 15 V at t=0.15 s. Figures 10 and 11 show the output-voltage and inductor-current responses, respectively.

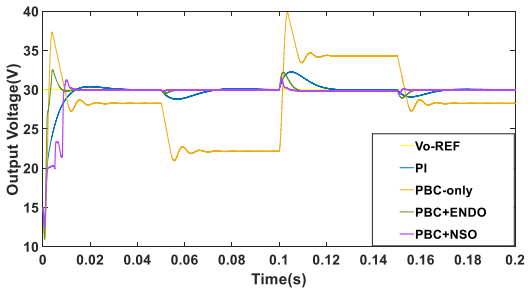


Fig. 10. Output voltage responses under input voltage variations (15 V → 12 V → 18 V → 15 V) in Scenario 4

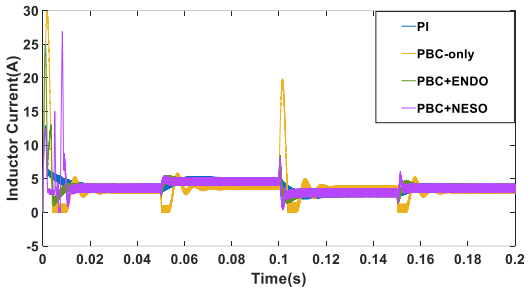


Fig. 11. Inductor current responses under input voltage variations (15 V → 12 V → 18 V → 15 V) in Scenario 4

Table 9. Output Voltage Performance Metrics Under Input-Voltage Variations in Scenario 4

Metric	PI	PBC-only	PBC+ ENDO	PBC+ NESO
Ts1 (ms)	18.911	N/A	3.566	0.501
PD1 (%)	4.14	30.234	1.641	0.826
MAE1 (V)	0.347	7.639	0.0668	0.0372
Ts2 (ms)	18.583	N/A	6.343	2.337
PD2 (%)	7.592	32.771	7.417	4.837
MAE2 (V)	0.526	4.631	0.296	0.177
Ts3 (ms)	15.911	N/A	5.670	1.567
PD3 (%)	3.169	14.374	3.585	2.100
MAE3 (V)	0.230	1.787	0.0963	0.0284

Table 9 summarizes the voltage-regulation metrics for the three transitions using the definitions introduced in Scenario 1. PBC-only does not satisfy the ±1% settling criterion within any of the three evaluation intervals. PBC+NESO yields the lowest reported PD and MAE values across all three transitions. Following the second and third transitions, it also achieves the shortest reported settling times: 2.337 and 1.567 ms, respectively, compared with 6.343 and 5.670 ms for PBC+ENDO.

Table 10 presents the integral voltage-error indices evaluated from the first input-voltage change at t=0.05 s to the end of the simulation. PBC+NESO yields the lowest reported IAE, ITAE, ISE, and ITSE among the four controllers. Together, these results indicate improved output-voltage regulation for PBC+NESO relative to the other tested controllers under the specified input-voltage transitions and loading conditions.

Table 10. Integral Voltage Error Indices Under Input Voltage Variations

Index	PI	PBC-only	PBC+ENDO	PBC+NESO
IAE	0.05516	0.70284	0.02295	0.01213
ITAE	0.00299	0.03795	0.00151	0.00083
ISE	0.06444	4.29585	0.01813	0.00357
ITSE	0.00333	0.17959	0.00111	0.00022

Practical Considerations for Inductor-Current Transients

The current excursions in Figs. 5, 7, 9, and 11 arise during startup and subsequent load, reference-voltage, or input-voltage changes. These events should be distinguished because their physical origins and current-mitigation requirements differ. In Figs. 5 and 9, the scheduled load changes alter the required steady-state current, with transient excursions superimposed on this adjustment.

Startup transients: All four figures exhibit initial current excursions before the scheduled disturbances. These belong to the startup response rather than the subsequent disturbance-rejection response. Their magnitude depends on the initial converter and controller states, including observer states in the observer-assisted implementations. When the output capacitor is initially below its operating voltage, capacitor charging also contributes to the startup energy demand. However, the plotted initial peaks should not be equated directly with source-connection inrush, which depends on the physical charging path, connection sequence, and initial capacitor voltage.

A practical startup sequence for a conventional boost converter can include current-limited precharge with the main power switch off and PWM disabled. The output capacitor then charges through the input–inductor–diode path toward the input voltage, subject to path drops and load conditions. A precharge resistor with a bypass arrangement or an active inrush-current limiter is needed to limit current in this path; disabling PWM alone does not provide this limitation. Following precharge, PWM operation can be enabled and the output-voltage reference increased gradually, with explicit startup current limiting and consistent controller–observer initialization. Load enablement, particularly for the CPL, should be coordinated with the available output voltage. This sequence separates current-limited precharge from subsequent controlled boost operation.

Reference-voltage transition: In Fig. 7, the reference increases from 24 to 36 V at t = 0.10 s. This commanded transition requires additional capacitor energy and increases the resistive-load power demand, while the resulting current excursions depend on the closed-loop dynamics. For $C = 1000\,\mu F$, the capacitor-energy difference between the target operating points is

$$\Delta \mathrm{E_C} = \frac{1}{2}\mathrm{C}(36^2 - 24^2) = 0.36\,\mathrm{J}$$

This value quantifies the capacitor-energy requirement of the desired transition; it neither determines the peak current nor establishes the actual energy change achieved by every controller. The peak magnitude and duration depend on the control law, tuning, reference trajectory, and any implemented current constraints. Reference-rate limiting combined with explicit current limiting can mitigate current stress, with a trade-off between current limitation and voltage-transition speed.

Input-voltage transition: In Fig. 11, the prominent positive current peak following the 12-to-18 V input transition at t = 0.10 s occurs with PBC-only. According to the averaged inductor dynamics, an input-voltage increase raises the inductor-current slope for unchanged duty ratio and output voltage; the subsequent trajectory depends on the closed-loop response. The pronounced PBC-only excursion accompanies its poorer voltage regulation in Fig. 10 and Table 9. This comparison concerns the tested controller implementations and does not isolate the absence of an observer as the sole cause of their differences. At a regulated output voltage and fixed load, increasing the input voltage reduces the ideal steady-state input-current requirement. The positive peak therefore represents a transient excursion rather than increased steady-state demand.

Current limits and protection: The physical interpretation of these transients does not establish their acceptability for a particular converter. Practical assessment requires checking peak magnitude, duration, repetition rate, and RMS current against inductor saturation characteristics, semiconductor current and safe-operating-area limits, and thermal constraints. Depending on the implemented protection scheme, these excursions may trigger a protective shutdown or engage cycle-by-cycle current limiting if the sensed current meets the corresponding threshold and timing conditions.

The present ideal-model simulation study evaluates voltage-regulation performance without a hardware prototype or specified component ratings and protection settings. Consequently, compliance with hardware current limits and overcurrent-protection activation were not assessed. Practical implementation requires coordination between startup management, current limiting, and protection. Validation should assess startup and subsequent disturbance intervals separately, using time-resolved current measurements with sufficient bandwidth to capture switching-related current stress. The suggested mitigation measures have not been evaluated in this study; their effects on voltage recovery and closed-loop stability require further investigation.

Taken together, the results of Scenarios 1-4 confirm that the proposed PBC+NESO controller achieves the best overall balance of transient performance, voltage-regulation accuracy, and disturbance rejection among the compared methods. Although the proposed controller-observer structure introduces additional tuning parameters relative to the PI and standalone PBC controllers and entails moderately greater design complexity than PBC+ENDO, this increase is justified by the consistently superior closed-loop performance observed across the test scenarios. In particular, the proposed method provides shorter settling times, lower voltage overshoots, lower mean absolute errors, and reduced cumulative voltage-error indices under CPL power changes, reference-voltage variations, parallel resistive-load disturbances, and input-voltage perturbations. Therefore, these results indicate that the proposed PBC+NESO strategy

offers a favorable trade-off between controller complexity and closed-loop robustness for boost converters supplying mixed resistive and CPL loads.

IV. Conclusion

This paper proposed a nonlinear extended state observer (NESO)-assisted passivity-based control strategy for a boost converter supplying parallel resistive and constant-power loads in DC microgrids. The proposed controller combines passivity-based energy shaping and damping injection with online estimation and compensation of lumped disturbances, thereby enhancing voltage-regulation accuracy and disturbance-rejection capability under load and source variations. For the reported gains and tested scenarios, the implemented PBC+NESO controller achieves the best overall balance of transient performance, voltage-regulation accuracy, and disturbance rejection among the evaluated configurations. This improvement is reflected in shorter settling times, lower voltage overshoots, lower mean absolute errors, and reduced cumulative voltage error indices across the tested CPL power changes, reference-voltage variations, parallel resistive-load disturbances, and input-voltage perturbations. For instance, following the first CPL step change, the proposed controller limited the output-voltage overshoot to 1.44% and achieved a settling time of 1.87 ms. Under the stated assumptions and within the specified operating region, the stability analysis further established the boundedness of all closed-loop signals and the uniform ultimate boundedness of the tracking and observer estimation errors. Future work will focus on experimental validation, investigation of digital implementation effects such as sampling and computation delays, systematic observer gain tuning, and extension of the proposed approach to multi-converter DC microgrid systems.

References

[1] T. Dragičević, X. Lu, J. C. Vasquez, and J. M. Guerrero, “DC Microgrids—Part II: A Review of Power Architectures, Applications, and Standardization Issues,” IEEE Transactions on Power Electronics, vol. 31, no. 5, pp. 3528–3549, May 2016, doi: 10.1109/TPEL.2015.2464277.

[2] L. Xu, J. M. Guerrero, A. Lashab, B. Wei, N. Bazmohammadi, J. C. Vasquez, “A Review of DC Shipboard Microgrids—Part I: Power Architectures, Energy Storage, and Power Converters,” IEEE Transactions on Power Electronics, vol. 37, no. 5, pp. 5155–5172, Nov 2021, doi: 10.1109/TPEL.2021.3128417.

[3] F. S. Al-Ismail, “DC Microgrid Planning, Operation, and Control: A Comprehensive Review,” IEEE Access, vol. 9, pp. 36154-36172, 2021, doi: 10.1109/ACCESS.2021.3062840.

[4] F. S. Al-Ismail, “A Critical Review on DC Microgrids Voltage Control and Power Management” IEEE Access, vol. 12, pp. 30345-30361, Feb 2024, doi: 10.1109/ACCESS.2024.3369609.

[5] A. Riccobono and E. Santi, “Comprehensive Review of Stability Criteria for DC Power Distribution Systems,” IEEE Transactions on Industry Applications, vol. 50, no. 5, pp. 3525-3535, Sep-Oct. 2014, doi: 10.1109/TIA.2014.2309822.

[6] A. Emadi, A. Khaligh, C. H. Rivetta, and G. A. Williamson, “Constant Power Loads and Negative Impedance Instability in Automotive Systems: Definition, Modeling, Stability, and Control of Power Electronic Converters and Motor Drives,” IEEE Transactions on Vehicular Technology, vol. 55, no. 4, pp. 1112-1125, July 2006, doi: 10.1109/TVT.2006.877483.

[7] D. Chatterjee, S. Kapat, I. Narayan Kar, and M. Bhowmik, “ Discrete-Time State Feedback Design Approach in a Digitally Current Mode Controlled Boost Converter for Improving Transient Performance and Stability,” IEEE Transactions on Power Electronics, vol. 40, no. 11, pp. 16740-16751, Nov. 2025, doi: 10.1109/TPEL.2025.3578346.

[8] M. A. Vaghela and M. A. Mulla, “High Step-Up Gain Converter Based on Two-Phase Interleaved Coupled Inductor Without Right-Hand Plane Zero,” IEEE Transactions on Power Electronics, vol. 38, no. 5, pp. 5911–5925, May 2023, doi: 10.1109/TPEL.2023.3239553.

[9] M. Leoncini, A. Dago, A. Bertolini, A. Gasparini, S. Levantino, and M. Ghioni, “A Compact High-Efficiency Boost Converter With Time-Based Control, RHP Zero-Elimination, and Tracking Error Compensation,” IEEE Transactions on Power Electronics, vol. 38, no. 3, pp. 3100-3113, Mar. 2023, doi: 10.1109/TPEL.2022.3222613.

[10] P. Melillo, M. Leoncini, S. Levantino, and M. Ghioni “Insights on the Dynamic Performance of Nonminimum-Phase Boost Converters Exploiting Inductor-Current-Feedback RHPZ Mitigation,” IEEE Transactions on Power Electronics, vol. 39, no. 4, pp. 4160-4172, Apr. 2024, doi: 10.1109/TPEL.2024.3352275.

[11] H. Gholizadeh and S. Hasanpour,“A New Quadratic CUK-Based Step-Up DC/DC Converter Without Right Hand Plane Zero,” International Journal of Industrial Electronics, Control and Optimization, vol. 8, no. 1, pp. 25–35, 2025, doi: 10.22111/ieco.2024.48683.1565.

[12] M. S. Sadabadi, X. Meng, and Z. Liu " Resilient and Robust Voltage Regulation in Shipboard DC Microgrids With ZIP Loads Under Actuator and Parameter Uncertainties," IEEE Transactions on Transportation Electrification, vol. 12, no. 1, pp. 578-588, Feb. 2026, doi: 10.1109/TTE.2025.3619129.

[13] M. A. Hassan, C. L. Su, J. Pou, G. Sulligoi, D. Almakhles, D. Bosich, and J. M. Guerrero, "DC Shipboard Microgrids With Constant Power Loads: A Review of Advanced Nonlinear Control Strategies and Stabilization Techniques," IEEE Transactions on Smart Grid, vol. 13, no. 5, pp. 3422 - 3438, Sep 2022. doi: 10.1109/TSG.2022.3168267.

[14] Z. Wang, and J. Hu,"Composite Sliding Mode Control for Converters With Unknown Constant Power Load," IEEE Transactions on Industry Applications, vol. 60, no. 3, pp. 4098-4108, June 2024, doi: 10.1109/TIA.2024.3360375.

[15] C. Zhang, M. Li, L. Zhou, C. Cui, and L. Xu, "A Variable Self-Tuning Horizon Mechanism for Generalized Dynamic Predictive Control on DC/DC Boost Converters Feeding CPLs," IEEE Journal of Emerging and Selected Topics in Power Electronics, vol. 11, no. 2, pp. 1650-1660, 2023, doi: 10.1109/JESTPE.2022.3225264.

[16] M. A. Hassan, C. L. Su, F. Z. Chen, and K. Y. Lo, " Adaptive Passivity-Based Control of a DC–DC Boost Power Converter Supplying Constant Power and Constant Voltage Loads," IEEE Transactions on Industrial Electronics, vol. 69, no. 6, pp. 6204-6214, Jun. 2022, doi: 10.1109/TIE.2021.3086723.

[17] M. Cao, S. Li, J. Yang, and K. Zhang, "Mismatched Disturbance Compensation Enhanced Robust H∞ Control for the DC-DC Boost Converter Feeding Constant Power Loads,"

IEEE Transactions on Energy Conversion, vol. 38, no. 2, pp. 1300-1310, June. 2023, doi: 10.1109/TEC.2022.3226472.
[18] W. Luo, T. Shi, A. Marquez, J. I. Leon, L. Wu, L. G. Franquelo, "Observer-Based Passivity Control for DC/DC Power Converters With Constant Power Loads," IEEE Transactions on Industrial Electronics, vol. 73, no. 1, pp. 1394-1402, Jan. 2026, doi: 10.1109/TIE.2025.3603031.
[19] F. Li and Z. Lin, "Novel passive controller design for enhancing boost converter stability in DC microgrid applications," IEEE Journal of Emerging and Selected Topics in Power Electronics, vol. 9, no. 6, pp. 6901-6911, Dec. 2021, doi: 10.1109/JESTPE.2021.3070234.
[20] A. M. Mohammadi, N. R. Abjadi, and G. R. Arab Markadeh,"Novel Modeling and Nonlinear Control of the Siwakoti-H Inverter Considering Flying Capacitor Voltage Balance for Photovoltaic Applications," International Journal of Industrial Electronics, Control and Optimization, vol. 8, no. 3, pp. 333–341, 2025, doi: 10.22111/ieco.2025.50965.1658.
[21] D. Ginoya, P. D. Shendge, and S. B. Phadke, "Sliding mode control for mismatched uncertain systems using an extended disturbance observer," IEEE Transactions on Industrial Electronics, vol. 61, no. 4, pp. 1983–1992, Apr. 2014, doi: 10.1109/TIE.2013.2271597.
[22] M. Abdolahi, J. Adabi, and S. Y. Mousazadeh Mousavi, "A passivity control and developed nonlinear disturbance observer for boost converter with constant power load in DC microgrid," International Journal of Circuit Theory and Applications, vol. 52, no. 11, pp. 5859–5876, Mar. 2024, doi: 10.1002/cta.4042.

Appendix A

Derivation and Validity of the Observer Lyapunov Estimate

This appendix derives the observer Lyapunov estimate in (58) and provides explicit admissible constants in terms of the observer gains and disturbance-rate bounds. The disturbance channels are understood to be locally absolutely continuous, with $\dot{d}_i = h_i$; consequently, derivative inequalities hold almost everywhere when the disturbance-rate inputs are measurable.

A. Exact Decomposition of the Observer-Error Dynamics

Using the error definitions in (48) and (50), the channel-wise observer-error dynamics in (51) are

$$\dot{\varepsilon}_\mathrm{i} = \eta_\mathrm{i} - \beta_{1\mathrm{i}}\mathrm{fal}(\varepsilon_\mathrm{i})$$
$$\dot{\eta}_\mathrm{i} = -\beta_{2\mathrm{i}}\mathrm{fal}(\varepsilon_\mathrm{i}) - \mathrm{h_i(t)},\ \mathrm{i}=1,2 \quad \text{(A.1)}$$

The disturbance-rate assumption in (46) gives

$$|h_i(t)| < \bar{h}_i,\ \mathrm{i}=1,2 \quad \text{(A.2)}$$

Here, $\bar{h}_i$ bounds the disturbance rate $\dot{d}_i = h_i$, rather than the disturbance amplitude.

define:

$$\mathrm{r_i}(\varepsilon_\mathrm{i}) = \mathrm{fal}(\varepsilon_\mathrm{i}) - \mathrm{c}_\delta\varepsilon_\mathrm{i},\ \mathrm{c}_\delta = \delta^{\alpha-1} > 0, \mathrm{i} = 1,2 \quad \text{(A.3)}$$

For the correction function in (49),

$$\mathrm{r_i}(\varepsilon_\mathrm{i}) = \begin{cases} 0 & ,\ |\varepsilon_\mathrm{i}| \le \delta \\ |\varepsilon_\mathrm{i}|^{\alpha}\mathrm{sgn}(\varepsilon_\mathrm{i}) - \mathrm{c}_\delta\varepsilon_\mathrm{i}, & |\varepsilon_\mathrm{i}| > \delta \end{cases} \quad \text{(A.4)}$$

Let

$$\mathrm{z_i} = \begin{bmatrix}\varepsilon_\mathrm{i} \\ \eta_\mathrm{i}\end{bmatrix},\ \mathrm{a_i} = \beta_{1\mathrm{i}}\mathrm{c}_\delta,\ \mathrm{b_i} = \beta_{2\mathrm{i}}\mathrm{c}_\delta \quad \text{(A.5)}$$

Substitution of (A.3) into (A.1) gives

$$\dot{\mathrm{z}}_\mathrm{i} = \mathrm{A_{oi}z_i} + \psi_\mathrm{i} \quad \text{(A.6)}$$

where

$$A_{oi} = \begin{bmatrix}-\mathrm{a_i} & 1 \\ -\mathrm{b_i} & 0\end{bmatrix},\ \psi_\mathrm{i} = \begin{bmatrix}-\beta_{1\mathrm{i}}\mathrm{r_i}(\varepsilon_\mathrm{i}) \\ -\beta_{2\mathrm{i}}\mathrm{r_i}(\varepsilon_\mathrm{i}) - h_i(t)\end{bmatrix} \quad \text{(A.7)}$$

using the observer-error vector $\theta = [\varepsilon_1 \quad \eta_1 \quad \varepsilon_2 \quad \eta_2]^T$ defined in (52), the stacked dynamics become

$$\dot{\theta} = A_o\theta + \Psi_o(\theta, t) \quad \text{(A.8)}$$

with

$$A_o = diag(A_{o1}, A_{o2}),\ \Psi_o(\theta,t) = \begin{bmatrix}\psi_1 \\ \psi_2\end{bmatrix} \quad \text{(A.9)}$$

equation (A.8) is an exact decomposition of the nonlinear observer-error dynamics; no nonlinear terms have been omitted.

B. Bounds on the Residual and Disturbance Contribution

Suppose that known uniform residual bounds hold over the trajectories and time interval under consideration:

$$\left|r_i\left(\varepsilon_i(t)\right)\right| \le \bar{r}_i\ ,\ \mathrm{i} = 1,2 \quad \text{(A.10)}$$

for a uniform ultimate-boundedness conclusion, these bounds and the disturbance-rate bounds must hold for all $\mathrm{t} \ge \mathrm{t}_0$, with constants common to the considered family of trajectories and independent of the initial time.

From (A.2), (A.7), and (A.10),

$$\|\Psi_o(\theta,t)\|^2 = \sum_{i=1}^{2}\left[{\beta_{1i}}^2{r_i}^2 + (\beta_{2i}r_i + h_i)^2\right] \le$$
$$\sum_{i=1}^{2}\left[{\beta_{1i}}^2{\bar{r}_i}^2 + \left(\beta_{2i}\bar{r}_i + \bar{h}_i\right)^2\right] = {\bar{\Psi}_o}^2 \quad \text{(A.11)}$$

where $\mathrm{r_i} = \mathrm{r_i}\left(\varepsilon_\mathrm{i}(\mathrm{t})\right)$ and $h_i = h_i(t)$.

Residual bounds can be computed on a prescribed error region

$$D_E = \{\theta \in \mathbb{R}^4 : |\varepsilon_i| \le E_i, i = 1,2\},\quad \mathrm{E_i} > 0 \quad \text{(A.12)}$$

an exact maximum-magnitude bound on this region is

$$\bar{\mathrm{r}}_\mathrm{i} = \begin{cases} 0 & ,0 < \mathrm{E_i} \le \delta \\ \mathrm{c}_\delta\mathrm{E_i} - {\mathrm{E_i}}^{\alpha}, & \mathrm{E_i} > \delta \end{cases} \quad \mathrm{i}=1,2 \quad \text{(A.13)}$$

to establish (A.13), note that for $\mathrm{s} \ge \delta$ and $0 < \alpha < 1$,

$$\mathrm{c}_\delta\mathrm{s} - \mathrm{s}^{\alpha} \ge 0$$

and

$$\frac{\mathrm{d}}{\mathrm{ds}}(\mathrm{c}_\delta\mathrm{s} - \mathrm{s}^{\alpha}) = \mathrm{c}_\delta - \alpha\mathrm{s}^{\alpha-1} \ge (1-\alpha)\mathrm{c}_\delta > 0$$

Consequently, when $\mathrm{E_i} > \delta$, the maximum residual magnitude is attained at $|\varepsilon_i| = E_i$.

If $\mathrm{E_i} \le \delta$ for both channels, the residuals vanish throughout $\mathrm{D_E}$, and

$${\bar{\Psi}_o}^2 = {\bar{\mathrm{h}}_1}^2 + {\bar{\mathrm{h}}_2}^2 \quad \text{(A.14)}$$

The regional bounds in (A.13) are valid only while the trajectory remains in $\mathrm{D_E}$. A sufficient condition ensuring continued validity of both the plant operating region and the observer residual region is provided in Appendix B.

C. Lyapunov Construction and Explicit Constants

The characteristic polynomial of A_{oi} is $\mathrm{s}^2 + \mathrm{a_i s} + \mathrm{b_i}$. Since $\mathrm{a_i}, \mathrm{b_i} > 0$, each $\mathrm{A_{oi}}$, and hence $\mathrm{A_o}$, is Hurwitz. For any selected symmetric positive-definite matrix $\mathrm{Q_o}$, there exists a unique symmetric positive-definite matrix $\mathrm{P_o}$ satisfying

$${A_o}^T P_o + P_o A_o = -Q_o \quad \text{(A.15)}$$

Consider

$$V_o = \theta^T P_o \theta \quad \text{(A.16)}$$

Define

$$p_{min} = \lambda_{min}(P_o), \quad p_{max} = \lambda_{max}(P_o) = \|P_o\|_2, \quad q_o = \lambda_{min}(Q_o) \quad \text{(A.17)}$$

Then

$$p_{min}\|\theta\|^2 \le V_o \le p_{max}\|\theta\|^2 \quad \text{(A.18)}$$

Differentiating (A.16) along (A.8) gives

$$\dot{V}_o = \theta^T(A_o{}^T P_o + P_o A_o)\theta + 2\theta^T P_o \Psi_o = -\theta^T Q_o \theta + 2\theta^T P_o \Psi_o \le -q_o\|\theta\|^2 + 2p_{max}\bar{\Psi}_o\|\theta\| \quad \text{(A.19)}$$

For any $0 < \tau < q_o$, Young's inequality yields

$$2p_{max}\bar{\Psi}_o\|\theta\| \le \tau\|\theta\|^2 + \frac{p_{max}^2 \bar{\Psi}_o{}^2}{\tau} \quad \text{(A.20)}$$

Therefore,

$$\dot{V}_o \le -(q_o - \tau)\|\theta\|^2 + \frac{p_{max}^2 \bar{\Psi}_o{}^2}{\tau} \quad \text{(A.21)}$$

A family of admissible constants in (58) is thus

$$\lambda_o = q_o - \tau, \ \sigma_o = \frac{p_{max}^2 \bar{\Psi}_o{}^2}{\tau}, \ 0 < \tau < q_o \quad \text{(A.22)}$$

In particular, choosing $\tau = \frac{q_o}{2}$ gives

$$\lambda_o = \frac{q_o}{2} > 0, \ \sigma_o = \frac{2p_{max}^2}{q_o}\sum_{i=1}^{2}\left[\beta_{1i}{}^2 \bar{r}_i{}^2 + \left(\beta_{2i}\bar{r}_i + \bar{h}_i\right)^2\right] \ge 0 \quad \text{(A.23)}$$

This establishes (58) wherever the bounds used in (A.10)-(A.11) hold. The parameter τ is an auxiliary analysis parameter, not an additional observer gain.

From (A.18), the same estimate implies

$$\dot{V}_o \le -k_o V_o + \sigma_o, \ k_o = \frac{\lambda_o}{p_{max}} > 0 \quad \text{(A.24)}$$

If the assumed bounds remain valid for all $t \ge t_0$, the comparison principle gives

$$V_o(t) \le e^{-k_o(t-t_o)}V_o(t_o) + \frac{\sigma_o}{k_o}\left(1 - e^{-k_o(t-t_o)}\right) \quad \text{(A.25)}$$

Consequently,

$$\limsup_{t\to\infty} \|\theta(t)\| \le \sqrt{\frac{p_{max}\sigma_o}{p_{min}\lambda_o}} \quad \text{(A.26)}$$

For $\sigma_o > 0$, any radius strictly larger than the right-hand side of (A.26) gives an ultimate error bound. The corresponding entry time can be chosen uniformly over bounded initial-error sets for which the same disturbance-rate and residual bounds hold for all future time. If $\sigma_o = 0$, (A.18) and (A.25) instead establish exponential convergence to the origin within the stated domain of validity.

D. Closed-Form Dependence on the Observer Gains

An explicit construction is obtained by selecting

$$Q_o = I_4 \quad \text{(A.27)}$$

Then $P_o = \mathrm{diag}(P_1, P_2)$, where

$$P_i = \begin{bmatrix} \frac{1+b_i}{2a_i} & -\frac{1}{2} \\ -\frac{1}{2} & \frac{1+b_i+a_i^2}{2a_i b_i} \end{bmatrix} \quad \text{(A.28)}$$

To obtain this expression, write

$$P_i = \begin{bmatrix} u_i & v_i \\ v_i & w_i \end{bmatrix}$$

The equation $A_{oi}{}^T P_i + P_i A_{oi} = -I_2$ gives

$$-2a_i u_i - 2b_i v_i = -1, \ u_i - a_i v_i - b_i w_i = 0, \ 2v_i = -1$$

Their solution is (A.28), which therefore satisfies

$$A_{oi}{}^T P_i + P_i A_{oi} = -I_2 \quad \text{(A.29)}$$

Moreover,

$$(P_i)_{11} = \frac{1+b_i}{2a_i} > 0, \ \det(P_i) = \frac{(1+b_i)^2 + a_i^2}{4a_i^2 b_i} > 0 \quad \text{(A.30)}$$

Thus, each P_i, and consequently P_o, is positive definite.

Writing the entries of P_i as $p_{11,i}$, $p_{12,i}$ and $p_{22,i}$ its eigenvalues are

$$\lambda_\pm(P_i) = \frac{p_{11,i}+p_{22,i} \pm \sqrt{(p_{11,i}-p_{22,i})^2 + 4p_{12,i}{}^2}}{2} \quad \text{(A.31)}$$

Therefore,

$$p_{max} = \max_{i=1,2}\lambda_+(P_i), \ p_{min} = \min_{i=1,2}\lambda_-(P_i) \quad \text{(A.32)}$$

For $Q_o = I_4$, the choice in (A.23) becomes

$$\lambda_o = \frac{1}{2}, \ \sigma_o = 2p_{max}^2\sum_{i=1}^{2}\left[\beta_{1i}{}^2\bar{r}_i{}^2 + \left(\beta_{2i}\bar{r}_i + \bar{h}_i\right)^2\right] \quad \text{(A.33)}$$

Equations (A.5), (A.13), and (A.28)-(A.33) explicitly specify the dependence of the estimate on the observer gains, α, δ, the prescribed error-region bounds, and the disturbance-rate bounds.

The fixed value $\lambda_o = \frac{1}{2}$ results from the normalization $Q_o = I_4$; it does not imply gain-independent observer performance. The observer gains affect P_o, σ_o, the comparison decay coefficient $k_o = \frac{\lambda_o}{p_{max}}$, and the ultimate error bound.

E. Regional Validity and a Sufficient Invariance Condition

The preceding estimate applies when either:

1. the uniform residual bounds in (A.10) are explicitly assumed along the trajectories under consideration; or

2. a region supporting those bounds is shown to contain the trajectory for all future time.

For the second case, a sufficient certificate can be constructed using a Lyapunov sublevel set. Let

$$l_1 = [1 \quad 0 \quad 0 \quad 0]^T, \ l_2 = [0 \quad 0 \quad 1 \quad 0]^T$$

so that $\varepsilon_i = l_i^T\theta$. The weighted Cauchy–Schwarz inequality gives

$$|\varepsilon_i|^2 \le (l_i^T P_o^{-1} l_i)V_o \quad \text{(A.34)}$$

Define

$$c_E = \min_{i=1,2} \frac{E_i^2}{l_i^T P_o^{-1} l_i} \quad \text{(A.35)}$$

Every sublevel set

$$\mathrm{L_c} = \{\theta : \mathrm{V_o}(\theta) \le \mathrm{c}\},\ 0 < \mathrm{c} < \mathrm{c_E} \quad \text{(A.36)}$$

is contained in the interior of $\mathrm{D_E}$.

Compute σ_o using the regional residual bounds in (A.13), and define

$$\mathrm{V_\infty} = \frac{\sigma_o}{\mathrm{k_o}} = \frac{\mathrm{p_{max}}\sigma_o}{\lambda_o} \quad \text{(A.37)}$$

Suppose that

$$\max \mathrm{V_o}(\mathrm{t_o}), \mathrm{V_\infty} < \mathrm{c_E} \quad \text{(A.38)}$$

Then a constant c can be selected such that

$$\max \mathrm{V_o}(\mathrm{t_o}), \mathrm{V_\infty} < \mathrm{c} < \mathrm{c_E}$$

While the trajectory remains in $\mathrm{L_c}$, the regional residual bounds are valid, and (A.24) gives, on its boundary,

$$\dot{\mathrm{V}}_\mathrm{o} \le -\mathrm{k_o c} + \sigma_o < 0 \quad \text{(A.39)}$$

Equivalently, applying the comparison estimate up to a hypothetical first boundary-exit time gives

$$\mathrm{V_o}(\mathrm{t}) \le \mathrm{e}^{-\mathrm{k_o}(\mathrm{t}-\mathrm{t_o})}\mathrm{V_o}(\mathrm{t_o}) + \mathrm{V_\infty}\left(1 - \mathrm{e}^{-\mathrm{k_o}(\mathrm{t}-\mathrm{t_o})}\right) < \mathrm{c}$$

This contradicts reaching the boundary $V_o = c$. Hence, L_c is positively invariant. Under the stated assumptions, if (A.38) holds and $\theta(t_o) \in L_c$, the trajectory remains in D_E, and the residual bounds used in the derivation remain valid for all $\mathrm{t} \ge \mathrm{t_o}$. Consequently, (A.25)-(A.26) hold along these trajectories.

Condition (A.38) provides a sufficient invariant-region certificate. More generally, the estimates (A.25)-(A.26) apply whenever the stated residual bounds hold uniformly along the trajectories under consideration.

Appendix B

Regional Constants and Proof of Proposition 1

A. Composite Lyapunov Estimate

Let R_x be the operating region in Assumption 1. For constant $\mathrm{V_{ref}}$, define

$g = \frac{k_v}{1-u_n}, I^* = \frac{V_{ref}/R_n + P_n/V_{ref}}{1-u_n}$

so that (23) gives $x_{1d} = I^* - g e_2$. Introduce the regional bounds:

$$\bar{e}_2 = max\{V_{ref} - \underline{v}, \bar{X}_2 - V_{ref}\}$$
$$\bar{X}_d = |I^*| + g\bar{e}_2$$
$$\bar{e}_1 = \bar{X}_1 + \bar{X}_d \quad \text{(B.1)}$$
$$\bar{e} = \sqrt{\bar{e}_1^2 + \bar{e}_2^2}, Y = \sqrt{\bar{X}_2^2 + \bar{X}_d^2}$$

Thus, $\|e\| \le \bar{e}$ and $|y_p| \le Y\|e\|$.

The exact residuals associated with (25)–(26) are:

$\Delta_1 = d_1 + g\dot{x}_2, \Delta_2 = d_2 - \frac{\mathrm{u}-\mathrm{u_n}}{\mathrm{C}}\mathrm{e_1}$

Since $u \in [u_{min}, u_{max}] \subseteq [0,1]$, admissible bounds are

$$F_2 = \frac{\bar{X}_1}{C} + \frac{\bar{X}_2}{R_n C} + \frac{P_n}{C\underline{v}} + \bar{d}_2$$

$$\bar{U} = max\{|u_{min} - u_n|, |u_{max} - u_n|\} \quad \text{(B.2)}$$
$$D_1 = \bar{d}_1 + gF_2,\ D_2 = \bar{d}_2 + \frac{\bar{U}}{C}\bar{e}_1$$

where $|\dot{x}_2| \le F_2$ and $|\Delta_i| \le D_i$.

Define:

$q = u_n - k_p y_p + u_c, s_u = sat_{[u_{min}, u_{max}]}(q) - q$

And let

$s_0 = dist(u_n, [u_{min}, u_{max}])$

Using $\hat{d}_2 = d_2 + \eta_2$ and $\hat{x}_{1\varepsilon} \ge \varepsilon_u > 0$, one obtains

$$|u_c| \le \frac{C}{\varepsilon_u}(\bar{d}_2 + \|\theta\|)$$
$$|s_u| \le s_0 + k_p Y\bar{e} + \frac{C}{\varepsilon_u}(\bar{d}_2 + \|\theta\|) \quad \text{(B.3)}$$

The second inequality follows from

$\mathrm{dist}(\mathrm{q}, [\mathrm{u_{min}}, \mathrm{u_{max}}]) \le \mathrm{s_0} + |\mathrm{q} - \mathrm{u_n}|$

therefore, saturation is retained without assuming a separate uniform bound on the observer error.

The dissipative terms satisfy:

$$\alpha_v(\xi)e_2^2 + k_p y_p^2 \ge e^T \underbrace{\begin{bmatrix} k_p x_2^2 & -k_p x_2 x_{1d} \\ -k_p x_2 x_{1d} & k_p x_{1d}^2 + \alpha_0 \end{bmatrix}}_{M} e \ge c_0\|e\|^2,$$

$$c_0 = \frac{k_p \alpha_0 \underline{v}^2}{k_p Y^2 + \alpha_0} > 0 \quad \text{(B.4)}$$

Here, M is symmetric positive definite because $k_p > 0$, $\alpha_0 > 0$ and $x_2 \ge \underline{v} > 0$. In particular,

$det(M) = k_p \alpha_0 x_2^2 \ge k_p \alpha_0 \underline{v}^2 > 0,$

$tr(M) = k_p(x_2^2 + x_{1d}^2) + \alpha_0 \le k_p Y^2 + \alpha_0$

Consequently,

$\lambda_{min}(M) \ge \frac{det(M)}{tr(M)} \ge c_0$

A conservative admissible choice is:

$\alpha_0 = \frac{1}{R_n} + k_v - \frac{P_n}{\underline{v}^2}$

provided that this expression is positive.

Substitution of (B.1)-(B.4) into the saturated storage inequality (66) yields:

$$\dot{V}_p \le -c_0\|e\|^2 + c_1\|e\|\|\theta\| + c_2\|e\| \quad \text{(B.5)}$$

with:

$$c_1 = \frac{2CY}{\varepsilon_u},\ c_2 = LD_1 + CD_2 + Y(s_0 + k_p Y\bar{e} + \frac{2C\bar{d}_2}{\varepsilon_u}) \quad \text{(B.6)}$$

These conservative constants retain the structured residuals, regularization, and saturation; no exact disturbance cancellation is assumed.

Combining (B.5) with (58), and applying Young's inequalities:

$c_1\|e\|\|\theta\| \le \frac{c_0}{4}\|e\|^2 + \frac{{c_1}^2}{c_0}\|\theta\|^2$, $c_2\|e\| \le \frac{c_0}{4}\|e\|^2 + \frac{{c_2}^2}{c_0}$

gives:

$$\dot{V}_c \le -\frac{c_0}{2}\|e\|^2 - (\rho\lambda_o - \frac{{c_1}^2}{c_0})\|\theta\|^2 + \frac{{c_2}^2}{c_0} + \rho\sigma_o \quad \text{(B.7)}$$

This proves (70). The bounds:

$m_e\|e\|^2 + \rho p_{min}\|\theta\|^2 \le V_c \le M_e\|e\|^2 + \rho p_{max}\|\theta\|^2$

and $V_c \ge \frac{Ce_2^2}{2}$ establish (71a)-(71b).

Equations (B.1)-(B.6), together with Appendix A, make the gain dependence explicit. In particular, k_v affects both dissipation and the virtual-reference coupling, k_p affects dissipation and saturation, and the observer gains affect P_o and σ_o. The weight ρ is an analysis parameter rather than an implemented controller gain.

B. Sufficient Regional-Validity Condition

Let $E_1, E_2 > 0$ define the observer residual region in (A.12), and compute the residual bounds from (A.13), and then evaluate σ_o using (A.22) or (A.23). Suppose:
$m_v = min\{V_{ref} - \underline{v}, \bar{X}_2 - V_{ref}\} > 0, m_1 = \bar{X}_1 - |I^*| > 0$
Define:

$$c_{max} = min\{\frac{Cm_v^2}{2}, \frac{m_1^2}{2(1/L+g^2/C)}, \frac{\rho {E_1}^2}{(P_o^{-1})_{11}}, \frac{\rho {E_2}^2}{(P_o^{-1})_{33}}\} \quad (B.8)$$

Indeed,
$|e_2|^2 \le \frac{2V_c}{C}, |x_1 - I^*|^2 \le 2V_c(1/L + g^2/C)$
and the weighted Cauchy–Schwarz inequality gives:
$|\varepsilon_1|^2 \le \frac{(P_o^{-1})_{11}V_c}{\rho}, |\varepsilon_2|^2 \le \frac{(P_o^{-1})_{33}V_c}{\rho}$
Hence, $V_c \le c < c_{max}$ lies strictly within both the plant operating region and the observer residual region.
A sufficient condition for continued regional validity is:

$$max\{V_c(t_0), \frac{\bar{\delta}}{k}\} < c_{max} \quad (B.9)$$

Choose c strictly between these two sides. On $V_c = c$,
$\dot{V}_c \le -kc + \bar{\delta} < 0$
Equivalently, applying (71a) up to a hypothetical first exit contradicts reaching this boundary. Thus, the sublevel set is positively invariant, provided the assumed disturbance bounds hold uniformly on the operating region and the usual solution-continuation conditions apply.



Mohammad Zabihi Laharami received the B.Sc. degree in electrical engineering from the University of Mazandaran, Iran, in 2010, and the M.Sc. degree in electrical engineering with a specialization in control from Babol Noshirvani University of Technology, Babol, Iran, in 2014. He is currently working toward the Ph.D. degree in electrical power engineering at Babol Noshirvani University of Technology, where he began his doctoral studies in 2022. His research interests include power electronics, nonlinear control, microgrids, and renewable energy systems. His methodological interests include model predictive control, fuzzy logic control, disturbance estimation, and bio-inspired optimization algorithms for power electronics applications.



Hoda Ghoreishy received her Ph.D. degree, specializing in power electronics and motor drives, from Tarbiat Modares University, Tehran, Iran, in 2012 in Electrical Engineering.
She is currently an Associate Professor with the Faculty of Electrical and Computer Engineering, Babol Noshirvani University of Technology, Babol, Iran. Her main research interests include modeling, analysis, design, and control of power electronic converters. Her area of interest also includes embedded software development for power electronics and electric drives using microcontrollers and DSPs.



Seyyed Yousef Mousazadeh Mousavi (Senior Member, IEEE) was born in Babol, Iran, in 1987. He received the B.Sc. degree with highest honors from the University of Mazandaran, Iran, in 2010, the M.Sc. degree from Amirkabir University of Technology, Iran, in 2012, and the Ph.D. degree from Iran University of Science and Technology, Iran, in 2018, all in Electrical Power Engineering. In 2016, he was a Visiting Ph.D. Student with the Department of Energy Technology, Aalborg University, Aalborg, Denmark. He joined the University of Mazandaran, Babolsar, Iran, as an Assistant Professor in September 2019 and was promoted to Associate Professor in 2026. His main research interests include microgrids, smart grids, distributed generation systems, power quality, and power electronics.